JM PAPERS

Large-eddy simulation of the tip vortex flow in a ducted propulsor

Theo J. T. Leasca[1,2] , **Thomas B. Kroll**[3] **and Krishnan Mahesh**[2]

[1]Naval Surface Warfare Center Carderock Division, West Bethesda, MD, USA

[2]Naval Architecture & Marine Engineering, University of Michigan, Ann Arbor, MI, USA

[3]Aerospace Engineering & Mechanics, University of Minnesota, Minneapolis, MN, USA

Corresponding author: Krishnan Mahesh, krmahesh@umich.edu

Large-eddy simulation (LES) is performed to study the tip vortex flow in a ducted propulsor geometry replicating the experiments of Chesnakas & Jessup (2003, pp. 257–267), Oweis *et al.* (2006*a J. Fluids Engng* **128**, 751–764) and Oweis *et al.* (2006*b J. Fluids Engng* **128**, 751–764). Inception of cavitation in these marine propulsion systems is closely tied to the unsteady interactions between multiple vortices in the tip region. Here LES is used to shed insight into the structure of the tip vortex flow. Simulation results are able to predict experimental propeller loads and show agreement with laser Doppler velocimetry measurements in the blade wake at design advance ratio, $J = 0.98$. Results show the pressure differential across the blade produces a leakage vortex which separates off the suction side blade tip upstream of the trailing edge. The separation sheet aft of the primary vortex separation point is shown to take the form of a skewed shear layer which produces a complex arrangement of unsteady vortices corotating and counterrotating with the primary vortex. Blade tip boundary layer vortices are reoriented to align with the leakage flow and produce instantaneous low-pressure regions wrapping helically around the primary vortex core. Such low-pressure regions are seen both upstream and downstream of the propeller blade trailing edge. The trailing edge wake is found to only rarely have a low-pressure vortex core. Statistics of instantaneous low pressures below the minimum mean pressure are found to be concentrated downstream of the blade's trailing edge wake crossing over the primary vortex core and continue in excess of 40 % chord length behind the trailing edge. The rollup of the leakage flow duct boundary layer behind the trailing edge is also seen to produce counter-rotating vortices which interact with the primary leakage vortex and contribute to strong stretching events.

Key words: turbulence simulation, vortex interactions, cavitation

T.J.T. Leasca, T.B. Kroll and K. Mahesh

1. Introduction

Rotating propeller blades are used to produce thrust in marine engineering applications by creating a pressure differential between the upstream and downstream sides of the blade. A tip vortex forms on any finite span blade when the high pressure on the downstream side of the propeller drives flow up and over the blade tip to where the pressure is much lower. Some propeller designs may enclose the rotating blades in a stationary duct or shroud, which allows for increased loading of the propeller. In such ducted propulsor rotors, the pressure differential between the suction and pressure sides of the blade near the tip is increased, which increases thrust and efficiency when the propeller diameter is constrained. As a result, the amount of circulation that must be shed in the blade tip vortices also increases.

Marine propeller design is constrained by cavitation, which is the process of liquid water transitioning to vapour in regions below the vapour pressure. Cavitation can generate unwanted noise, lead to structural vibrations and cause material erosion. The inception of cavitation is a fundamentally three-dimensional and unsteady process, motivating the need for high-fidelity modelling. The tip vortex is frequently a location of global minimum pressure, making it a likely place for cavitation inception to occur.

To observe tip vortex cavitation inception in ducted propulsors, two geometrically similar three-bladed propellers P5407 (smaller) and P5206 (larger) were studied in the experiments by Judge *et al.* (2001), Chesnakas & Jessup (2003), Oweis *et al.* (2006*a*) and Oweis *et al.* (2006*b*). An important motivation of this experimental campaign was to understand the Reynolds number scaling of tip vortex inception in ducted propulsors and its difference from open propellers. The flow in the tip vortex region was measured with laser Doppler velocimetry (LDV). Vortex circulation and core radius were reconstructed from the LDV measurements and vortex core pressure was inferred by fitting a Rankine vortex model. The primary tip vortex separates from the blade surface upstream of the trailing edge as a result of the stronger leakage flow in the ducted propulsor. The primary tip vortex also interacts with secondary vortical structures near the blade trailing edge. These flow structures were termed the tip-leakage vortex and trailing-edge vortex. The mutual interaction of these vortices was observed to be related to cavitation inception, which was found to occur farther downstream than the location of minimum mean core pressure. It was hypothesised by Chesnakas & Jessup (2003) that inception events occur when the weaker trailing edge vortex is wrapped around the stronger tip leakage vortex before eventually merging farther downstream. Small-scale vortical structures were thought to undergo strong stretching in this merger process which generates the very low pressures driving inception. Examination of the instantaneous flow fields in Oweis *et al.* (2006*a*) found evidence for this hypothesis, with multiple corotating and counter-rotating vortices observed in the LDV measurements behind the trailing edge. Oweis *et al.* (2006*b*) studied the smaller P5407 rotor outside the duct configuration, finding that the open rotor has a stronger tip leakage vortex than the ducted rotor. Saraswat *et al.* (2024) performed stereo particle image velocimetry measurements of a two-bladed ducted propeller of similar pitch, rake and skew to P5407 and confirmed the presence of multiple corotating and counter-rotating secondary vortices around the primary tip-leakage vortex. Saraswat *et al.* (2024) notes that the number, location and strength of trailing vortices depends on the propeller advance ratio.

Propeller P5206 has been studied computationally using Reynolds-averaged Navier–Stokes by Brewer (2002), Kim *et al.* (2006), Hsiao & Chahine (2006) and Hsiao & Chahine (2008). It was found that the predicted location of minimum mean pressure was close to the blade tip at 10 % of the chord length downstream. Since the computed locations of

mean low-pressure were not coincident with experimental inception observations, it was concluded that unsteady vortex interactions should be resolved to capture the resulting low-pressure fluctuations.

The fluid dynamics of ducted propulsors are also closely related to those of axial fans and waterjet pumps. Such turbomachinery flows have been studied experimentally by Wu *et al.* (2011*b*, 2012) and Miorini *et al.* (2012). They note that turbulence around the leakage vortex is highly anisotropic with various sources and regions of production. Of particular importance is the observation that the jetting shear layer from the suction side blade tip produces new vortex filaments, and transports them to the primary leakage vortex core. These filaments were observed to spiral around the primary tip-leakage vortex before getting entrained.

In the present work, large-eddy simulation (LES) is used to study the flow around P5407 at design advance ratio. The objectives of this study are to (i) assess and illustrate the ability of LES using an unstructured overset method to predict flow over a ducted propeller in the design condition, (ii) provide insight into the tip-region vortex interactions, (iii) examine statistics of extreme low-pressure events necessary for cavitation inception.

The paper is organised as follows. The numerical method, geometry discretisation and simulation boundary conditions are detailed in § 2. Section 3.1 introduces the simulation results with qualitative comparisons of the global flow features with previous research. Section 3.2 validates simulation results with comparisons with integrated loads and LDV flow field measurements at the blade trailing edge. Section 3.3 provides discussion of the instantaneous LES results on the finest mesh. Additional complexity in the flow field not observed by Chesnakas & Jessup (2003) and Oweis *et al.* (2006*a*) is revealed. Statistics of intermittent low-pressure events likely to lead to cavitation inception are presented in § 3.4. Finally, § 3.5 uses the time-average LES to investigate the flow features that drive the production of small-scale vortices observed in the instantaneous flow field in § 3.3. New instability mechanisms in ducted propulsor tip flows not discussed in the previous literature are identified and their importance is revealed by analysis of the Reynolds shear stresses.

2. Approach

2.1. *Numerical method*

Here LES is performed using an unstructured overset method. The LES resolves a wide range of turbulent length and time scales to capture the transient behaviour of tip vortex interactions. The use of overset grids provides additional flexibility in the grid generation process by allowing meshes to overlap and move in relation to each other. This flexibility also allows for increased resolution with nearly orthogonal hexahedral control volumes in relevant areas near the propeller blades, duct and tunnel walls while coarsening away from the blade. The incompressible Navier–Stokes equations are solved in an arbitrary Lagrangian–Eulerian formulation where the grid velocity is included in the convection term. The moving mesh approach to simulating propeller rotation is chosen so that future simulations could more easily incorporate other blade elements such as, for example, stationary inlet guide vanes (Kroll & Mahesh 2022). In general, each component overset grid can have a different angular velocity or acceleration. Inclusion of the grid velocity in the convection term therefore avoids having to track multiple reference frames.

The filtered Navier–Stokes equations with the arbitrary Lagrangian–Eulerian formulation are as follows:

$$\frac{\partial \overline{u}_i}{\partial t} + \frac{\partial}{\partial x_j}(\overline{u}_i \overline{u}_j - \overline{u}_i V_j) = -\frac{\partial \overline{p}}{\partial x_i} + \nu \frac{\partial^2 \overline{u}_i}{\partial x_j \partial x_j} - \frac{\partial \tau_{ij}}{\partial x_j},$$

$$\frac{\partial \overline{u}_i}{\partial x_i} = 0, \tag{2.1}$$

where u_i is the velocity in the inertial frame, p is the pressure, ν is the kinematic viscosity, V_j is the grid velocity, the overbar $\overline{(\cdot)}$ denotes the spatial filter and $\tau_{ij} = \overline{u_i u_j} - \overline{u}_i \overline{u}_j$ is the subgrid stress tensor. The subgrid stress is modelled using the dynamic Smagorinsky model

$$\tau_{ij} = \nu_T \left(\frac{\partial \overline{u}_i}{\partial x_j} + \frac{\partial \overline{u}_j}{\partial x_i}\right) = \nu_T \overline{S_{ij}}, \tag{2.2}$$

$$\nu_T = C_s^2 \Delta^2 |\overline{S_{ij}}|, \tag{2.3}$$

proposed by Germano *et al.* (1991) and modified by Lilly (1992), where ν_T is the eddy viscosity, Δ is the grid filter width and C_s is dynamically computed from the solution itself. The Lagrangian time scale is dynamically computed based on a surrogate – correlation of the Germano – identity error (Park & Mahesh 2009). This approach has shown good performance for a variety of marine propeller flows (Verma & Mahesh 2012; Kumar & Mahesh 2017).

Equation (2.1) is solved using a finite volume segregated predictor–corrector scheme developed in Mahesh *et al.* (2004). Cartesian velocities and pressure are stored at cell centroids while face-normal velocities are stored separately for face centroids. The interpolation between centroid and face velocities is performed in a manner that emphasises discrete kinetic energy conservation (Mahesh *et al.* 2004). The grid velocity V_j is assumed to be linear between time steps and reconstructed from the difference in centroid locations between the current and previous time step. Cartesian pressure gradients at the centroids are computed using a least-squares formulation. Face values and face-normal gradients required for the finite volume flux evaluations are computed using a nodal reconstruction where the node values are obtained by least-squares from the surrounding cell centroid values. Linear basis functions are then used to integrate the nodal values across the face, as detailed by Horne & Mahesh (2021). At overset grid boundaries, values are interpolated from overlapping meshes using a supercell such that the volume integral of interpolated quantities are conserved (Horne & Mahesh 2019a,b). The pressure Poisson equation is solved monolithically for all overset grids. The face normal gradient of pressure is enforced to be zero on all domain boundaries and mass conservation across overset grid interpolation fringes is enforced using a Courant penalty force (Horne & Mahesh 2019b). The approach has been validated for a variety of marine flows (Kroll *et al.* 2020; Morse & Mahesh 2021; Kroll & Mahesh 2022; Morse & Mahesh 2023a,b)

2.2. *Geometry and discretisation*

The Propeller 5407 blade and duct geometry is shown in figure 1. The duct has a uniform cross-section from the inflow to the rotor hub's aft edge. The coordinate x is the direction along the propeller rotation axis, with $x = 0$ representing the nominal rotor disk, located at the blade root midchord. Positive values of x are taken to be downstream of the rotor plane such that the bulk flow through the duct has a positive sign of axial velocity. The azimuthal coordinate θ is normalised as $s = R\theta/c$ where R is the propeller tip radius and c is the chord length, which is constant along the span. The azimuthal coordinate origin $\theta = 0$ is taken be the blade tip trailing edge such that positive values ($s > 0$) are behind the blade. Using the right-hand rule, the propeller rotates in the negative θ direction
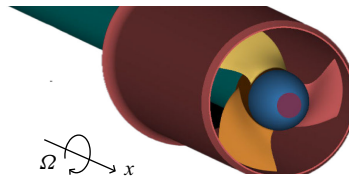
1010 A51-4

Figure 1. Visualisation of the three-bladed propeller P5407 and bellmouth duct. Note that x is the axial direction along the propeller axis; Ω is the propeller rotation, here being clockwise around the x axis. Using the right-hand rule, the propeller rotates in the negative θ direction, such that positive $s = R\theta/c$ is behind the blade trailing edge.
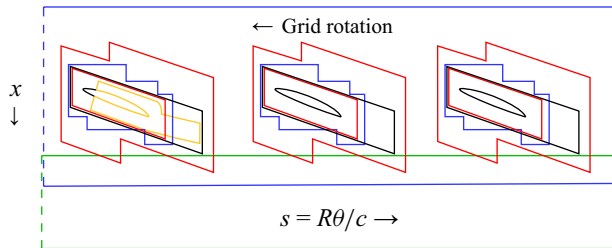

Figure 2. Illustration of the overset grid structure used for P5407 in $x - \theta$ space. Lines denote the boundaries of each overset grid. In order of from finest resolution to coarsest: the gold illustrates the tip refinement region (Blade 1 only), black illustrates the near blade, red is the blade shroud, blue is the blade buffer and green is the hub wake. Dashed lines indicate the boundary around the azimuth between $\theta = -\pi$ and $\theta = \pi$.

with angular velocity $\Omega = \mathrm{d}\theta/\mathrm{d}t$. More details of the propeller geometry including pitch, rake and skew distributions are provided in Oweis *et al.* (2006*a*,*b*).

The numerical grid is composed entirely of hexahedral cells. The use of the overset method allows local control of mesh quality and resolution. Figure 2 illustrates the boundaries of the various overset meshes in $x - \theta$ space, with the dashed lines indicating the continuous boundary between $\theta = -\pi$ and $\theta = \pi$ in the azimuthal direction. The most refined mesh is the body-fitted grid copied rotationally for each of the three individual blades of P5407, with boundaries displayed in black. The outer section of the grid in the radial direction is extended $0.5c$ in the downstream θ direction from the propeller blade tip. This is done to maintain the high resolution of the near-blade mesh in the region of the tip vortices trailing behind the blade. The blade grid also resolves the full tip gap between the blade and duct walls without any overset interpolation boundary.

To transition from the high-resolution near-blade mesh to the far field background grid, three layers of intermediate-resolution grids are introduced. Ratios of control volume edge lengths in the overset interpolation fringe are limited to $3:1$ in each direction. The cell edge length aspect ratio in the overset fringe is limited to a maximum of 5. The first transition grid is illustrated in red in figure 2. It originates just inside the near-blade mesh and surrounds each of the three individual blades, and is repeated three times. The second transition grid is illustrated in blue and originates just inside the outer boundary of the first transition mesh surrounding each of the three blades. The second transition grid extends around the azimuth. The final transition mesh is displayed in green and provides refinement of the hub boundary layer and wake before transitioning to the background mesh at the outlet of the duct. All grid boundaries are constructed such that no cutting is performed in the solver to remove redundant control volumes. The wall-normal spacings and growth rates are equivalent between all overset meshes to provide accurate interpolation of the turbulent boundary layer flow.

	Grid 1	Grid 2	Grid 3
Number of processors	7260	12 032	9088
Number of CVs ($\times 10^6$)	178	560	227
Tip gap resolution ($h/\Delta r$)	40	62	73
Chordwise resolution ($c/R\Delta\theta$)	330	476	630
Time step ($\Delta t U_\infty/R$)	8×10^{-5}	4×10^{-5}	2×10^{-5}

Table 1. Comparison of resolutions and mesh partitioning for the three grids considered in the present LES. Here CVs is the number of control volumes, Δr denotes the grid cell size in the radial direction, $R\Delta\theta$ denotes the grid cell size in the chordwise direction.
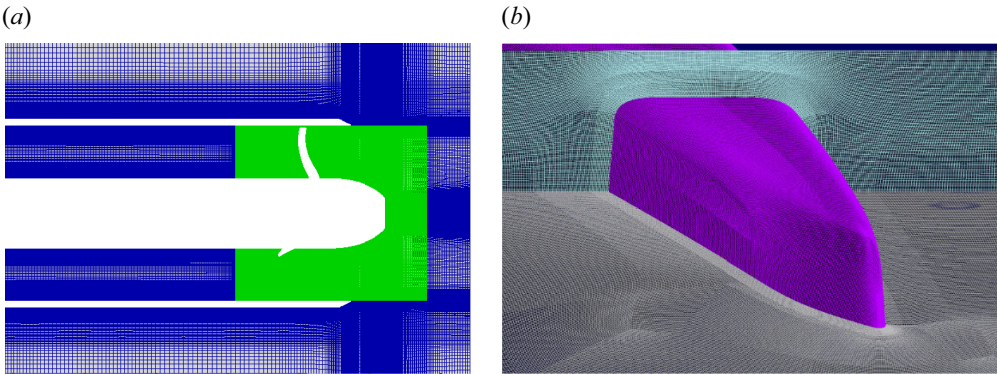
Figure 3. (*a*) A slice showing the grid for the three-bladed propeller P5407 with a duct. The background grid (blue) and all the overset grids (green). White space represents the negative volume inside the shaft blade and duct solid geometries. (*b*) Cuts through the tip refinement overset used in Grid 3. The blade tip surface mesh at the trailing edge is shown in purple; cyan is an $x-r$ slice across the tip gap; grey is an $x-\theta$ slice.

Two levels of resolution are considered for the background and transition meshes, with a refinement ratio of approximately 1.5. As detailed in table 1, the coarse grid (termed 'Grid 1' hereafter) resolves the blade chord with 330 control volumes from leading edge to trailing edge. Forty control volumes span the gap between the blade tip and duct. The total number of control volumes in Grid 1 is 178×10^6. The fine mesh ('Grid 2' hereafter) uses 476 control volumes along the blade chord and 62 control volumes across the tip gap for a total cell count of 560×10^6.

The third computational mesh ('Grid 3') presented here adds an additional overset on top of the coarse grid to provide highly local resolution in the blade tip only. As illustrated in gold in figure 2, the tip refinement begins one-quarter along the blade chord, and closely follows the tip vortex trajectory behind the blade trailing edge. The tip refinement has 630 control volumes along the blade chord direction and 73 control volumes across the tip gap. As seen in table 1, Grid 3 has an overall cell count less than half that of the Grid 2, demonstrating the efficiency enabled by the overset method.

Figure 3 shows an $x-r$ slice through the grid with the background mesh shown in blue and the overset meshes shown in green. The narrow tip gap can be seen for one of the three blades above the shaft. Figure 3 shows an $x-r$ slice through the grid with the background mesh shown in blue and the overset meshes shown in green. The narrow tip gap can be seen for one of the three blades above the shaft. The gap distance between the blade tip and duct wall is $h/R = 0.0156$. Figure 3(*b*) shows cuts through Grid 3 at the blade tip trailing edge. The blade surface mesh is shown in purple. The mesh cut coloured in cyan roughly

corresponds to an $x-r$ plane showing the wall normal resolution in the tip gap. The mesh cut coloured in grey roughly corresponds to the $x-\theta$ plane. The isotropy of the grid in the $x-\theta$ plane is found to be important to allow secondary vortices inclined with respect to the primary leakage vortex to be captured regardless of the vortex core orientation. Defining the tip vortex core boundary as the isoline of mean vorticity $\langle\omega_\theta\rangle R/U_\infty = 50$, the number of computational control volumes spanning the mean vortex core is approximately 40, 60 and 80 for Grids 1, 2 and 3, respectively.

2.3. *Simulation set-up*

The inflow into the domain is located $4.2R$ upstream of the rotor disk at $x=0$ (the left-hand boundary seen in figure 3a). The computational inflow is placed just downstream of the experimental duct's bellmouth duct inlet to allow for precise control of the volumetric flow rate to the rotor. The inflow boundary condition is prescribed as a uniform value equal to the mean flow rate through the duct in the experiments of Chesnakas & Jessup (2003) and is equal to $U_{inf,BC} = 0.968U_\infty$, where U_∞ is the free stream velocity. The mean flow rate is found by integrating LDV measurements of the inflow profile taken at $x = -0.3615R$ where R is the propeller radius. The boundary layer is numerically tripped just downstream of the inflow plane at $x = -4R$ by applying a steady wall-normal velocity of 0.06 % of U_∞. This numerical tripping results in a fully turbulent inflow to the rotor. A convective boundary condition is set $4R$ downstream of the propeller centre in the outlet section. The blades and hub surfaces contained in the rotating grids are given the boundary condition $u_{face} = \Omega \times R$ while the duct surface is given a no-slip boundary condition $u_{face} = 0$. All other surfaces have no-slip boundary conditions. The Reynolds number considered here is

$$Re_{tip} = \frac{\sqrt{U_\infty^2 + (\Omega R)^2}c}{\nu} = 1.1 \times 10^6. \tag{2.4}$$

The non-dimensional time step used for Grid 1 is $\Delta t U_\infty/R = 8 \times 10^{-5}$. Grid 2 uses a non-dimensional time step of $\Delta t U_\infty/R = 4 \times 10^{-5}$. The non-dimensional time step of $\Delta t U_\infty/R = 2 \times 10^{-5}$ for Grid 3 results in an overall computational cost per propeller revolution that is similar between Grids 2 and 3 despite having approximately one half the total number of control volumes.

Averaging is performed over 3.5 revolutions after statistical steady state is reached. This sampling window is seen in § 3.2.2 to be sufficient for convergence of second-order flow statistics and loads. Conditional statistics for regions with pressure instantaneously below the minimum mean pressure are also collected. Sampling is performed at a non-dimensional time interval of $\Delta t U_\infty/R = 1.5 \times 10^{-3}$.

3. Results

3.1. *Qualitative description of the flow*

In this section, the global features of the flow are described. Figures 4(a) and 4(b) show photographs of developed vortex cavitation from the experiments of Chesnakas & Jessup (2003). Annotations on the figure detail the key flow features identified by Chesnakas & Jessup (2003) and Oweis *et al.* (2006a). The photograph is oriented looking down at the blade tip such that the blade rotation causes the tip to move upwards in the frame. The bulk flow through the duct moves in the positive x-direction, from left to right. The pressure gradient across the blade results in a leakage flow moving in the negative x-direction in the gap region between the blade and the duct. The leakage flow separates off the suction side
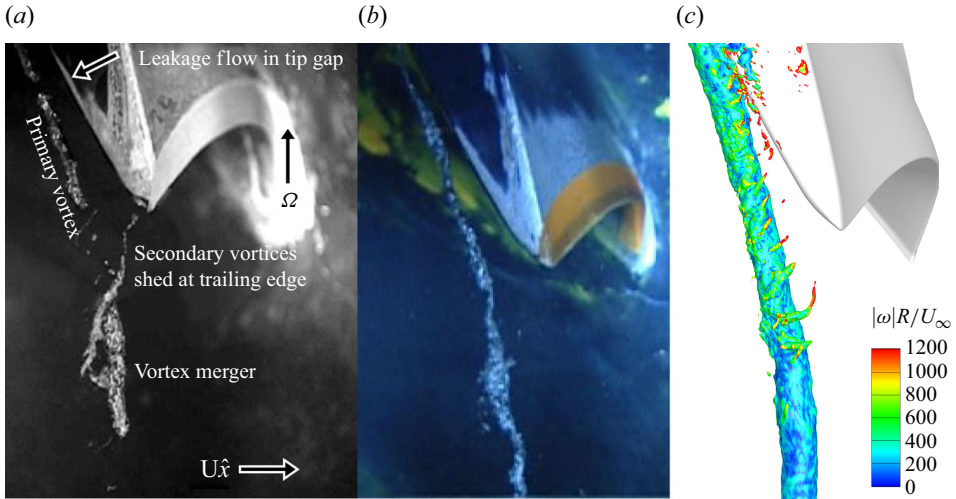
(*a*)   (*b*)   (*c*)

Figure 4. (*a*, *b*) Photograph of developed tip vortex cavitation from the experiments of Chesnakas & Jessup (2003) at $\sigma = 2(p_\infty - p_v)/(\rho U_\infty^2) = 5.6$. (*c*) Isosurface of instantaneous $C_p = -3.9$ from the current LES results on Grid 2 coloured by vorticity magnitude $|\omega| R/U_\infty$.

blade tip and rolls up into a coherent vortex, termed the primary leakage vortex hereafter. The primary leakage vortex core is seen to coincide with regions of vapour upstream from the trailing edge. Aft of the trailing edge, an additional vapour region coincides with the merger of secondary vortex structures from the trailing edge wake. The extent of the trailing edge vortex cavity differs between figures 4(*a*) and 4(*b*) suggesting that the trailing edge vortex cavitation is an intermittent process.

Figure 4(*c*) shows an isosurface demarcating a low-pressure coefficient region of $C_p < -3.9$ from the current LES simulation results. The pressure coefficient is defined as

$$C_p = \frac{p - p_\infty}{\frac{1}{2}\rho U_\infty^2}, \tag{3.1}$$

where p is the local pressure, p_∞ is the reference pressure, U_∞ is the free stream velocity and ρ is the fluid density. The reference pressure is taken as the time-averaged pressure inside the duct at midspan upstream of the rotor at $x = -3.5R$. The C_p isosurface in figure 4(*c*) is coloured by vorticity magnitude. The entire low-pressure region corresponds to a vorticity magnitude $|\omega| R/U_\infty > 200$. The low-pressure region follows a qualitatively similar trajectory to the primary leakage vortex observed to cavitate in figures 4(*a*) and 4(*b*). Additional qualitative similarities are seen in the orientation and location of secondary vortical structures of higher vorticity magnitude $|\omega| R/U_\infty > 600$ merging in the blade wake aft of the trailing edge. An in-depth discussion of the small-scale vortex structures near the trailing edge is presented later in § 3.3.

3.2. *Validation*

In this section, the time-averaged loads and flow fields from the LES simulations are validated against the experiments of Chesnakas & Jessup (2003), Oweis (2003) and Oweis *et al.* (2006*a*,*b*). Three-dimensional LDV data are provided by NSWCCD (Thad Michael, personal communication).

	EXP-1	EXP-2	EXP-3	LES-G1	LES-G2
Re_{tip}	1.4M	1.4M	1.4M	1.1M	1.1M
$\langle K_T \rangle$	0.278	0.245	0.265	0.273	0.274
$\langle K_Q \rangle$	0.053	0.054	0.054	0.054	0.054

Table 2. Comparison of load statistics for Propeller P5407 at $J = 0.98$ and $Re_{tip} = 1.1 \times 10^6$. Here EXP-1 is Chesnakas & Jessup (2003), EXP-2 is Oweis (2003) and EXP-3 is Oweis *et al.* (2006*b*). Here LES-G1 is the current simulation on Grid 1 and LES-G2 is the current simulation on Grid 2. Data from Chesnakas & Jessup (2003) was provided by NSWCCD (Thad Michael, personal communication).

3.2.1. *Loads*

The time-averaged load statistics from the LES at an advance ratio of $J = 0.98$ are compared with the experiments of Chesnakas & Jessup (2003), Oweis (2003), Oweis *et al.* (2006*a*) and Oweis *et al.* (2006*b*). The advance ratio is defined as

$$J = \frac{2\pi U_\infty}{\Omega D}, \tag{3.2}$$

where U_∞ is the free stream velocity, Ω is the rotational velocity in units of radians per second and D is the propeller diameter. The experiments of Chesnakas & Jessup (2003), Oweis *et al.* (2006*a*) and Oweis *et al.* (2006*b*) adopted the time-average velocity value midway between the hub and duct in the radial direction as U_∞. Note that $U_{inf,BC}$ prescribed at the simulation inflow is chosen such that the volumetric flow rate through the duct reproduced that of the corresponding experiments, as discussed in the preceding section. Table 2 summarises the mean loads, comparing the LES simulations to various experiments for propeller P5407. The thrust and torque coefficients are defined as

$$K_T = \frac{4\pi^2 T}{\rho \Omega^2 D^4}, \quad K_Q = \frac{4\pi^2 Q}{\rho \Omega^2 D^5}, \tag{3.3}$$

where T is the thrust force, Q is the torque and ρ is the fluid density. The difference between the LES loads on Grid 1 and Grid 2 is 1 % for K_T and less than that for K_Q, suggesting grid convergence of the integral circulation. The experimental load data for K_T from three different experiments contains some scatter with a difference of approximately 13 % of the K_T magnitude. For K_Q, one of the experimental values has a minor 2 % difference. For both Grids 1 and 2, the LES shows agreement with the experimental K_Q values and lying with in the scatter for K_T.

Loads are also measured at an advance ratio around $J = 1.1$ for P5407 and compared with the experimental data of Chesnakas & Jessup (provided by Thad Michael, personal communication). Measurements of the inflow were not available, making it difficult to precisely determine the duct mass flow and U_∞ for the calculation of the advance ratio, J. For that reason, a range of inflows velocities, $U_{inf,BC}$ are considered for the same propeller rotation rate corresponding to roughly $J = 1.1$. The data are plotted in figure 5 and shows that a 1.5 % reduction in $U_{inf,BC}$ results in a 13 % reduction in the thrust coefficient K_T. Such sensitivity dK_T/dJ matches the experimental results well. The sensitivity is also well predicted for dK_Q/dJ.

These results highlight the extreme load sensitivity to the inflow of ducted propulsors and to make the case that integral quantities such as volumetric flow rate are preferred relative to single-point inflow measurements for definition of the advance ratio J. This conclusion is especially important when comparisons are being made across different test set-ups with significantly different Reynolds numbers. Reynolds number variations modify the
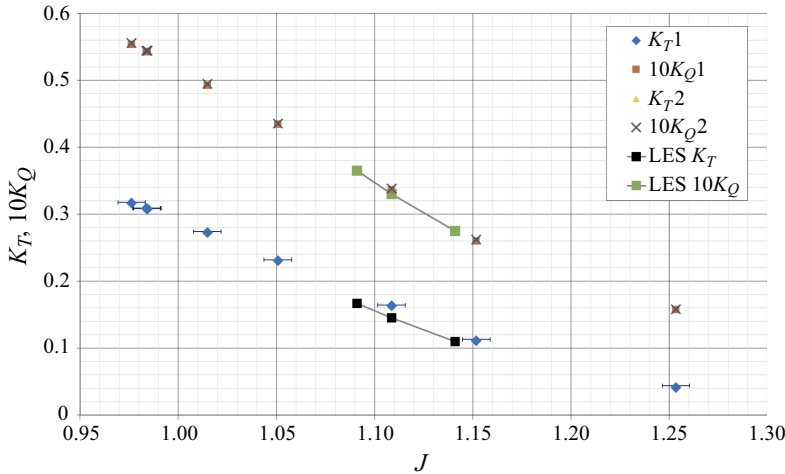
Figure 5. Force coefficients K_T and K_Q across range of J. The LES results for Grid 1 are superimposed on data from Chesnakas & Jessup (personal communication).

boundary layer thicknesses on both the shaft and the duct wall and may therefore result in a different midchannel velocity for the same mass flow rate. The same effect may also occur when changing propeller rotation rates within the same test set-up. Lower rotation rates than the 'nominal' condition at which the inflow is measured, such as that considered here, result in a reduction in the favourable pressure gradient experienced by the upstream boundary layer on both the duct and shaft. Weaker favourable pressure gradients result in a thickening of the boundary layer, causing the peak velocity at midspan to increase assuming the mass flow rate remains constant.

3.2.2. *Grid refinement and LDV comparisons*

The time-averaged flow statistics from the LES are compared with the three-dimensional LDV experimental data of Chesnakas & Jessup (2003) with extracts taken in the $x-r$ plane where the axial coordinate x and radial coordinate r are normalised by the propeller radius R. Chesnakas & Jessup (2003) state that the uncertainty in velocity measurements was 10 % of U_∞ at the vortex core location and in the blade wake. The cause of uncertainty was linked to inadequate sample sizes taken in regions of high turbulence. Figure 6 shows the LDV grid in figure 6(*a*) compared with LES numerical Grid 1 (figure 6*b*) and Grid 2 (figure 6*c*). The LES solution mesh extends farther towards the duct wall than the LDV with points clustered in the duct boundary layer.

Figure 7 compares contour slices of the mean axial velocity $\langle u_x \rangle / U_\infty$ in the $x-r$ plane at the blade trailing edge ($R\theta/c = 0$). The axial flow moves upstream (negative u_x in blue) above the propeller blade tip radius, which is termed the tip leakage flow. The axial flow moves in the positive x direction at values of the radial coordinate below the blade tip ($r/R < 1$). There are discrepancies in the LES and LDV results near the duct surface where the experimental viewing window protrudes into the circular duct cross-section and the LDV has a coarser resolution. The LES predicts a thinner boundary layer on the duct wall and larger magnitude of the reversed leakage flow velocity near $r/R = 1.01$. Some blade-to-blade scatter is seen in the extracted profiles of the LDV data. Grid convergence is seen between the three mesh resolutions in the mean axial flow velocity.

Figure 8 compares the azimuthal velocity u_θ / U_∞ in the inertial frame. The $x-r$ plane at the blade trailing edge is shown in $a-c$. The LDV measurements and LES simulations
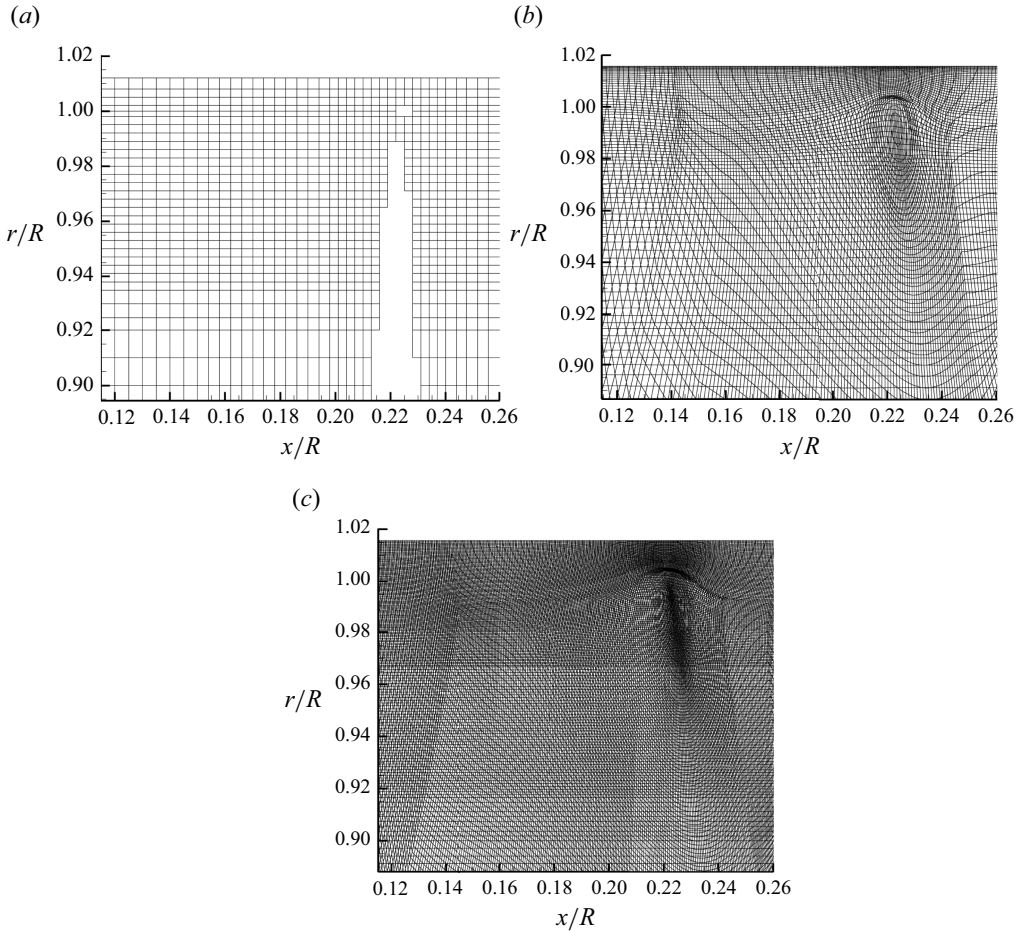
(a)

(b)

(c)

Figure 6. Grid resolutions in the $x-r$ plane at the blade trailing edge for (a) the LDV measurements of Chesnakas & Jessup (2003), (b) the present coarse LES Grid 1 and (c) present LES Grid 3.

with both grid resolutions show $u_\theta/U_\infty \approx 1$ in the leakage vortex lower periphery and separation sheet. The LDV measurements predict slightly negative azimuthal velocity in the vortex upper periphery and leakage flow, while both LES solutions show values near zero. The LES results underpredict the azimuthal velocity beneath the leakage vortex ($r/R < 0.94$) relative to the experimental measurements. In figure 8(d), profiles are extracted in the axial direction at $R\theta/c = 0.05$ to avoid the blanking region where the blade trailing edge obscures optical access. Good agreement is seen in the blade wake velocity deficit, though the blade wake thickness is overpredicted by LES relative to the LDV measurements.

The evolution of trailing vortices behind the blade trailing edge is shown in figure 9. Figure 9(a,d,g,j) show the measurements of mean azimuthal vorticity $\langle\omega_\theta\rangle R/U_\infty$ behind Blade 2 from the experiments of Chesnakas & Jessup (2003) at $R\theta/c = 0.0, 0.084, 0.167$ and 0.251. Figure 9(b,e,h,k) show the time average results on Grid 1 and figure 9(a,d,g,j) show the time average results from Grid 3 in the present LES. The vorticity is mostly directed in the positive θ direction (out of the page or anticlockwise using the right-hand rule) and peaks at the leakage vortex centre. The leakage vortex is formed from the rollup of the leakage flow separating off the blade suction side at a specific chord location before
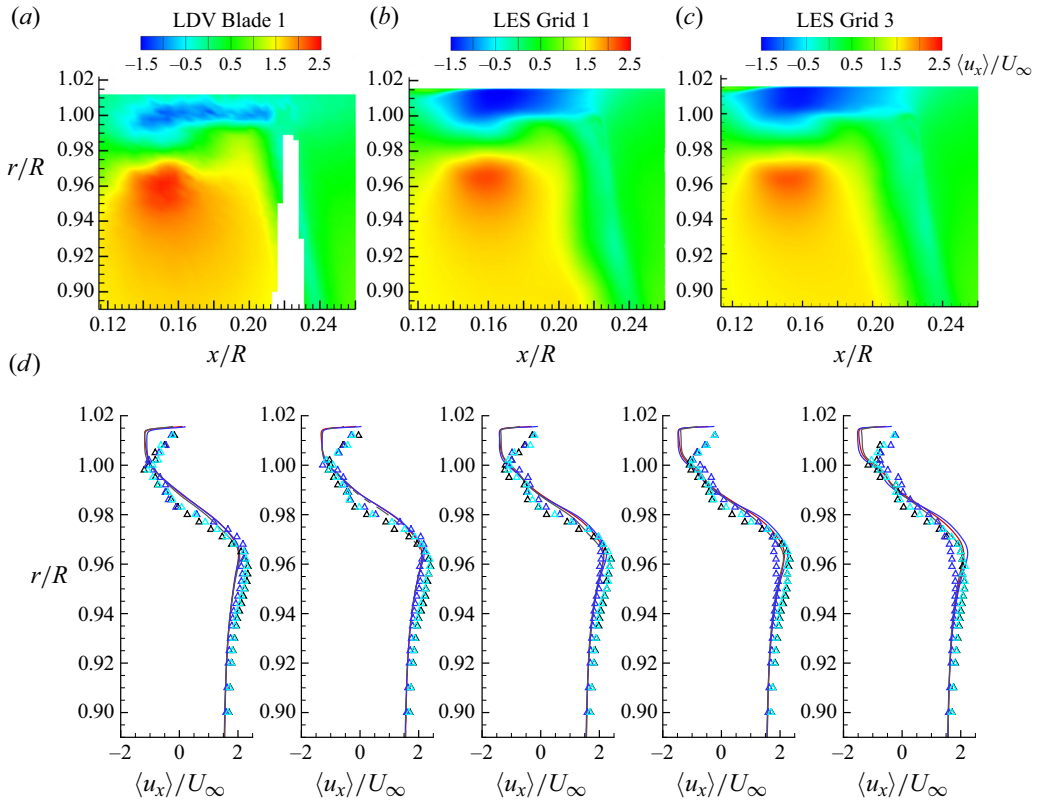
Figure 7. Contours of the mean axial velocity $\langle u_x \rangle / U_\infty$ in the $x-r$ plane at the blade trailing edge for (*a*) the LDV measurements of Chesnakas & Jessup (2003), (*b*) the present LES on Grid 1 and (*c*) present LES on Grid 3 profiles are extracted at $x/R =$ 0.145, 0.150, 0.154, 0.158 and 0.162 are shown in (*d*) for LES Grid 1 (—), LES Grid 2 (—), LES Grid 3 (—), LDV Blade 1 (△), LDV Blade 2 (△), LDV Blade 3 (△).

the blade trailing edge. The leakage vortex is therefore offset from the blade trailing edge into the negative axial direction. A separation sheet connects the leakage vortex core to the blade tip, visible as a narrow region of high vorticity of the same sign as the leakage vortex core. Wall shear of the reversed leakage flow induces counter-rotating vorticity on the duct wall (seen in orange). To the left of the leakage vortex core, the region of counter-rotating vorticity begins to grow away from the duct wall. The LDV data does not have sufficient resolution to capture the near-wall shear and this region of counter-rotating vorticity. Farther behind the blade at $R\theta/c = 0.084$, a second vortex corotating vortex is seen to the right of the primary leakage vortex in both the LDV (figure 9*d*) and LES (figure 9*e*, *f*). This secondary vortex forms behind the blade trailing edge in the rollup of the suction side blade wake and separation sheet. The trailing edge vortex is weaker than the primary leakage vortex. At $R\theta/c = 0.167$, the trailing edge vortex is directly on top of the leakage vortex core in both the LDV (figure 9*g*) and LES (figure 9*h*, *i*). The leakage vortex is flattened, with a larger region of high vorticity on the upstream (left-hand) side of the core than the right-hand side. Finally, at $R\theta/c = 0.251$ the trailing edge vortex begins to merge with the leakage vortex from the upstream periphery in both LDV (figure 9*j*) and LES (figure 9*k*, *l*) results. The counter-rotating vortex has separated from the duct wall in the LES. Overall, very strong agreement in the evolution of the trailing vortex system is seen between the LDV measurements and LES. Both LES grid resolutions predict similar
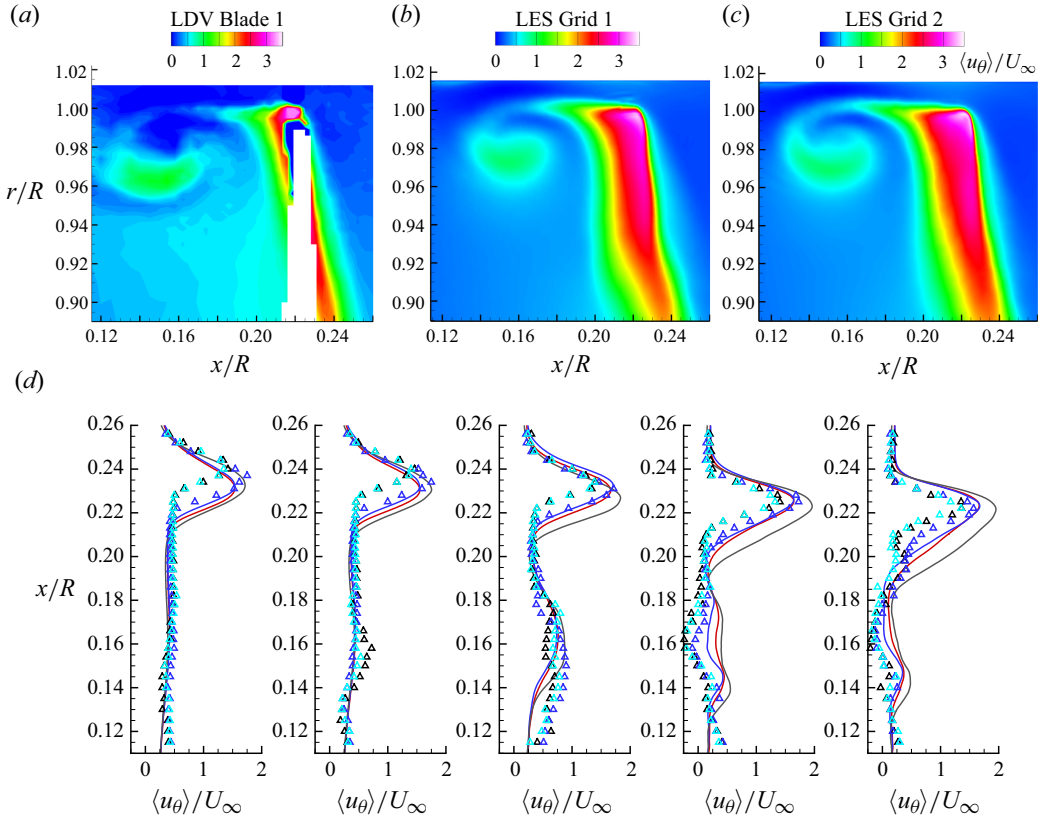
Figure 8. Contours of the mean azimuthal velocity $\langle u_\theta \rangle / U_\infty$ in the $x{-}r$ plane at the blade trailing edge for (*a*) the LDV measurements of Chesnakas & Jessup (2003) (*b*) the present LES on Grid 1 and (*c*) present LES on Grid 3. Profiles extracted at $R\theta/c = 0.05$ and $r/R =$ 0.944, 0.95, 0.968, 0.989 and 0.995 are shown in (*d*) for LES Grid 1 (——), LES Grid 2 (——), LES Grid 3 (——), LDV Blade 1 (△), LDV Blade 2 (△), LDV Blade 3 (△) .

rotation strengths and core trajectories for both the leakage and trailing edge vortex. The behaviour of the counter-rotating vorticity on the duct wall is also reproduced closely between the two grid resolutions shown.

For a more detailed comparison with the experiment, profiles are taken of $\langle \omega_\theta \rangle R/U_\infty$ in the $x{-}R$ plane at the blade trailing edge (figure 10*a*–*c*). The profiles move along the radial direction at various axial locations near the primary leakage vortex core. The three LES mesh resolutions are plotted as solid lines while the three individual blades from the LDV are plotted as symbols. The mean ω_θ peaks correspond closely and the LES results are within the experimental scatter. Differences near the duct wall surface are observed as previously discussed.

A comparison of the locations of the tip leakage vortex centre is shown in table 3. The leakage vortex centre is taken to be the location of the maximum mean vorticity. The vortex locations for the three individual blades in the LES mesh are all within 1 % of each other, evidence of statistical convergence. Some scatter is observed in the experimental results between the blades, with differences up to 6 % in the axial direction. The LES results agree best with the experimental results for Blade 3 within 1.3 % for the axial location and 0.6 % for the radial location.

As an assessment of the appropriateness of the mesh resolution, figure 11 shows a contour of eddy-viscosity ν_T normalised by the molecular viscosity ν in the tip vortex
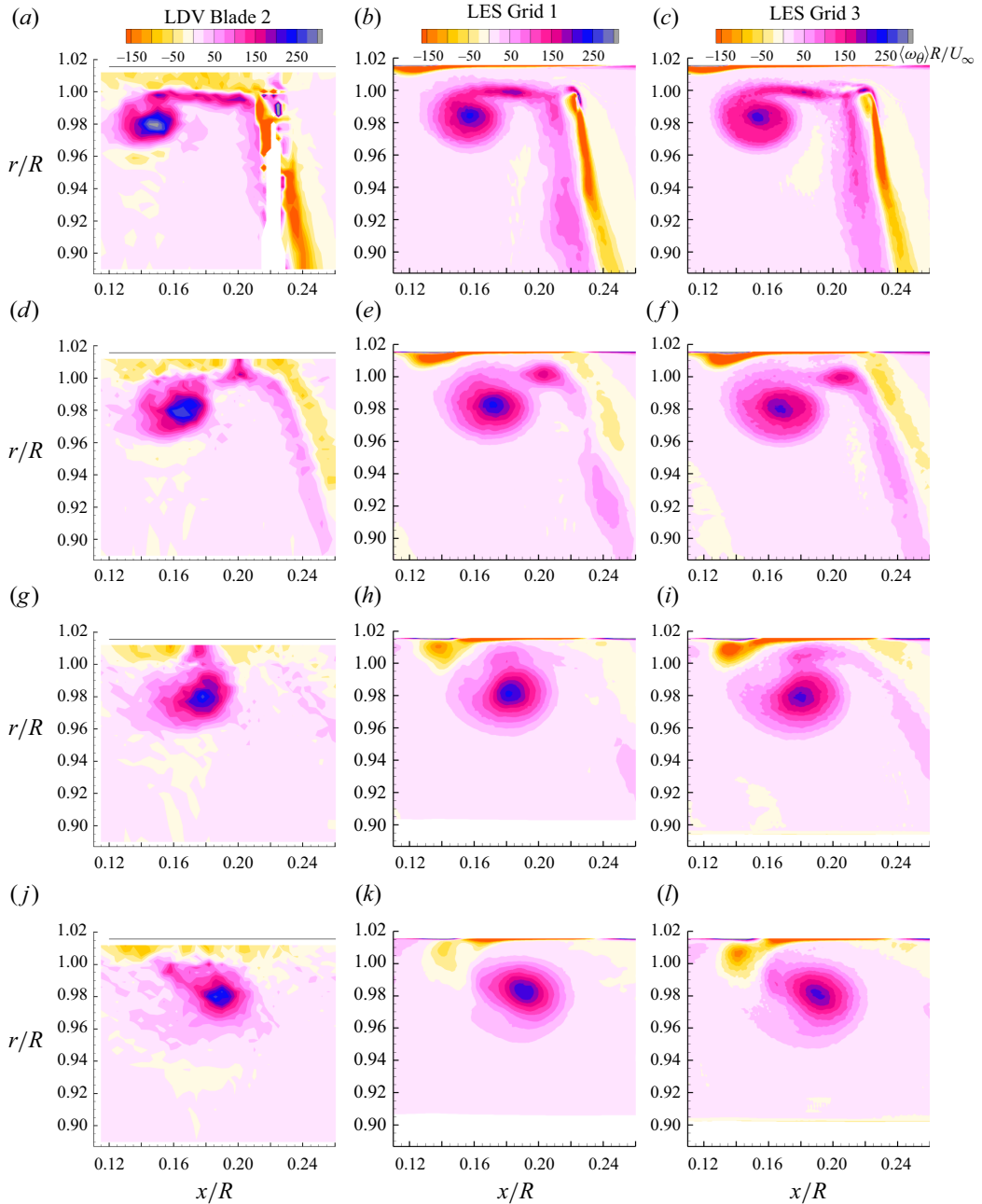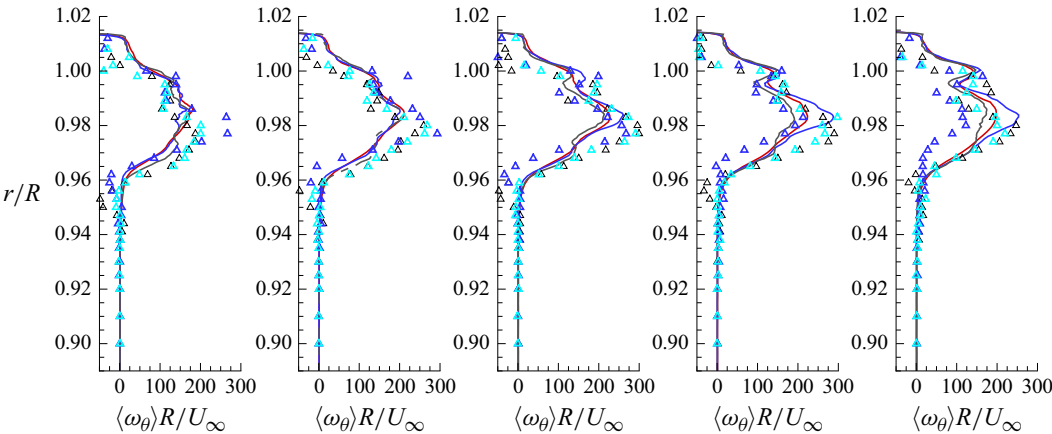
Figure 9. Contours of the mean azimuthal vorticity field in the $x-r$ planes behind the blade trailing edge at $R\theta/c = 0.00$ for (a, b, c), 0.084 (d, e, f), 0.167 (g, h, i), 0.251 (j, k, l). Panels (a,d,g,j) show the LDV measurements from Chesnakas & Jessup (2003) while (b,e,h,k) show the present LES on Grid 1 and (c,f,i,l) show present LES Grid 3.

region at the trailing edge ($R\theta/c = 0$). As seen in (2.1) and (2.2), the eddy viscosity is the parameter by which the subgrid-scale model influences the LES solution. The eddy viscosity ratio is therefore a measure of the unresolved turbulent scales and tends to zero

Figure 10. Profiles of the mean azimuthal vorticity $\langle\omega_\theta\rangle R/U_\infty$ in the $x-r$ plane at the blade trailing edge. Profiles extracted at $x/R =$ 0.145, 0.150, 0.154, 0.158 and 0.162 are shown in (*d*) for LES Grid 1(——), LES Grid 2(——), LES Grid 3 (——), LDV Blade 1 (△), LDV Blade 2 (△), LDV Blade 3 (△).

	EXP-1 Blade 1	EXP-1 Blade 2	EXP-1 Blade 3	LES-G1 Blade 1	LES-G1 Blade 2	LES-G1 Blade 3	LES-G2 Blade 1	LES-G2 Blade 2	LES-G2 Blade 3
x/R	0.154	0.148	0.157	0.158	0.158	0.159	0.159	0.158	0.159
r/R	0.979	0.980	0.977	0.984	0.983	0.983	0.983	0.983	0.983

Table 3. The $x-r$ plane mean tip leakage vortex centre locations and strength of the experiment of Chesnakas & Jessup (2003) Here EXP-1 compared with LES results for Grid 1 (LES-G1) and Grid 2 (LES-G2) grids.
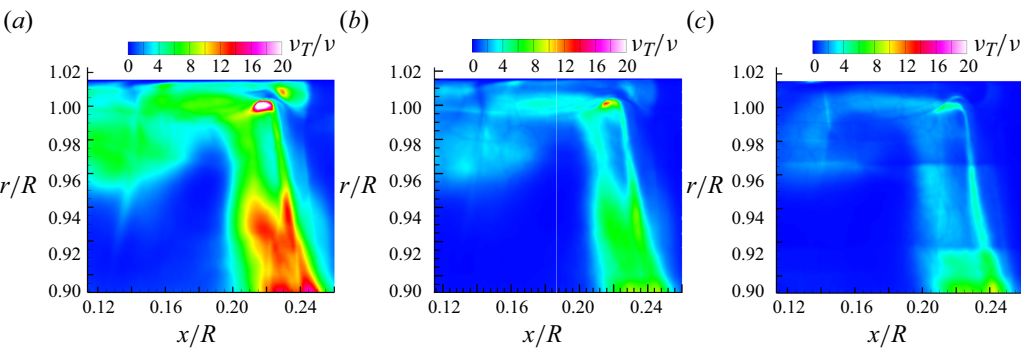

Figure 11. A contour slice in the $x-r$ plane at the propeller trailing-edge tip $R\theta/c = 0$ showing the LES eddy-viscosity ν_T normalised by the molecular viscosity ν for (*a*) Grid 1, (*b*) Grid 2 and (*c*) Grid 3.

as the grid is refined. Figure 11 shows that in the tip vortex interaction region, ν_T/ν has a maximum of approximately 6 for Grid 1, 3 for Grid 2 and 2 for Grid 3. This suggests sufficient resolution in the vortex interaction areas to minimise the LES subgrid model's influence on the observed flow structure.
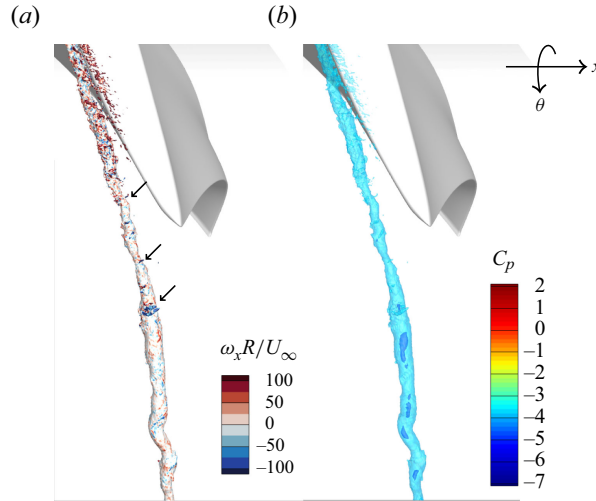
Figure 12. (*a*) Instantaneous isosurface of $Cp = -3.7$ coloured by axial vorticity $\omega_x R/U_\infty$.
(*b*) Instantaneous isosurfaces of $C_p = -5.5$ and -3.7 are displayed transparently and coloured by C_p.

3.3. *Instantaneous flow field*

This section provides an in-depth analysis of tip vortex flow structures and their relation to low-pressure events that drive cavitation inception. The instantaneous LES results on the finest discretisation (Grid 3) are examined.

Assessment of the instantaneous pressure field reveals the primary leakage vortex has an identifiable low-pressure region, visualised with an isocontour of $C_p = -3.7$ in figure 12. No coherent trailing edge vortex is captured in the trailing edge region by visualisation of the pressure field. However, side lobes of low pressure are seen wrapping helically around the primary leakage vortex core both forward and aft of the blade trailing edge. In figure 12(*a*), these side lobes are seen to correspond to areas of strong axial vorticity, while the primary leakage vortex core mostly aligns with the azimuthal direction, θ. The high axial vorticity is evidence that the side lobes seen in the pressure isosurface correspond to secondary vortex filaments with a core inclined with respect to the primary leakage vortex. This observation from the LES is consistent with high-speed video of cavitation inception from experimental tests of a similar propulsor by Saraswat *et al.* (2024). In figure 12(*b*), an isosurface of $C_p = -5.5$ is displayed in darker blue along with the transparent isocontour of $C_p = -3.7$ in cyan. It reveals that the leakage vortex core pressure continues to decrease aft the blade trailing edge in the θ direction. At the bottom of the image ($R\theta/c = 0.4$), a helical oscillation mode of the primary leakage vortex core is observed behind the blade.

Figure 13 displays an isosurface of $C_p = -4.7$ (transparent grey) along with isocontours of Q-criterion, revealing a more complex flow field of small-scale vortex structures. The Q-criterion is the second invariant of the velocity gradient tensor (Hunt *et al.* 1988), defined as

$$Q = \frac{1}{2}|\boldsymbol{\omega}| - S_{ij}S_{ij} = \frac{\partial u_i}{\partial x_j}\frac{\partial u_j}{\partial x_i}, \tag{3.4}$$

where S_{ij} is the velocity strain rate tensor and $\boldsymbol{\omega}$ is the vorticity vector. For incompressible flows, it can also be shown that
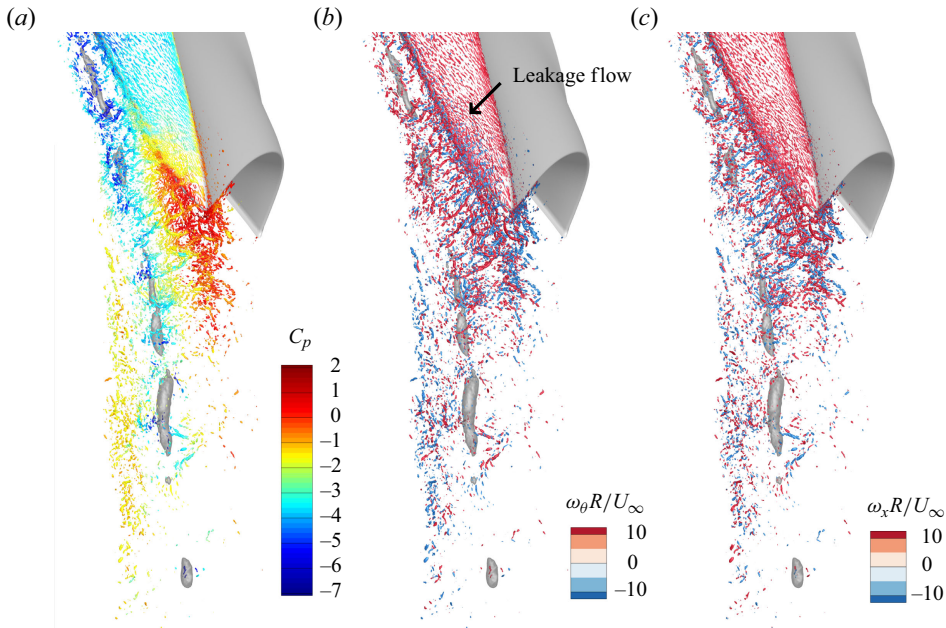
$$Q = \frac{1}{2\rho}\nabla^2 p, \tag{3.5}$$

Figure 13. Instantaneous isosurfaces of $QR^2/U_\infty^2 = 180000$ coloured in (*a*) by the pressure coefficient C_p, (*b*) by the azimuthal vorticity $\omega_\theta R/U_\infty$ and (*c*) by axial vorticity $\omega_x R/U_\infty$. An isosurface of $C_p = -4.7$ is also displayed in transparent grey to denote the location of the primary leakage vortex.

demonstrating that Q behaves as a source term for pressure (Dubief & Delcayre 2000). Figure 13 shows that the strongest instantaneous vortex structures are not colocated or aligned with the primary leakage vortex. The non-locality of high positive Q with global pressure minima is a consequence of the elliptic nature of the pressure Poisson equation, which results in changes to the pressure field acting over larger distances than the kinematic source term. This observation highlights the importance of rotation across both small and large scales to the lowest pressures driving cavitation inception.

In figure 13(*a*), isosurfaces of $QR^2/U_\infty^2 = 180\,000$ are coloured by the local pressure coefficient C_p. The trailing edge wake remains at a pressure higher than ambient (p_∞) and much higher than the pressure in the primary vortex core. This is evidence that, instantaneously, there are no coherent vortex structures at the trailing edge with strong enough rotation to induce a distinct low-pressure core. In figure 13(*b*), isosurfaces of Q are coloured by the sign of the azimuthal vorticity $\omega_\theta R/U_\infty$, revealing that the flow separating off the trailing edge is a mixture of small-scale vortices corotating (red) and counterrotating (blue) with the primary leakage vortex. These observations of the instantaneous LES results counter the description of the mean flow field given by Chesnakas & Jessup (2003) and shed additional insights on the descriptions of the instantaneous flow field given by Oweis *et al.* (2006*a*). In figure 13(*c*), isosurfaces of Q are coloured by the sign of the axial vorticity $\omega_x R/U_\infty$, and reinforce the observation of mixed positive and negative directions of rotation at the smallest scales.

The leakage flow aft of the midchord has a positive u_θ and negative u_x and thus moves from northeast to southwest as denoted by the black arrow in figure 13(*b*). Vortices generated in the blade tip boundary layer are seen in figures 13(*b*) and 13(*c*) to be oriented perpendicular to the leakage flow. Small-scale vortex filaments are present throughout the separation sheet connecting the blade tip to the primary leakage vortex core aft of the core separation point. Interestingly, the separation sheet is seen to have instantaneous

vortex structures that are aligned nearly parallel to the leakage flow. This observation indicates that the separation sheet is not simply transporting vorticity from the blade tip boundary layer. Rather, the shear of the separation sheet itself (discussed further in § 3.5.1) is dynamically relevant in the sense that the tip boundary layer vorticity gets tilted and deformed before being fed to the primary leakage vortex core. The orientation and placement of those leakage flow-aligned vortices in the separation sheet correspond to the previously discussed side lobes of low-pressure wrapping helically around the primary vortex core (figure 12).

After the blade passes, the vortex structures of the separation sheet and trailing edge wake then traverse over the top of the primary leakage vortex before meeting the incoming bulk flow through the duct, which moves from left to right in figure 13. The traverse process is influenced by the induced velocity of both the primary leakage vortex and its image, given the close proximity of the duct wall. Secondary vortex structures therefore have a short residence time in the region directly above the leakage vortex radially.

There is also an additional counter-rotating vortex visible to the left-hand side of the primary leakage vortex in figure 13(*b*). This counter-rotating vortex is located upstream in the axial direction and above the primary leakage vortex core in the radial direction and oriented nearly parallel to the primary vortex core. This upstream vortex results from the rollup of the duct boundary layer vorticity that occurs as the reversed leakage flow ($u_x < 0$) meets the turbulent inflow ($u_x > 0$). Similar behaviour was also observed in the waterjet pump experimentally studied by Wu *et al.* (2012). To examine this rollup further, the azimuthal vorticity field is plotted on $x-r$ slices in figure 14(*a*). The primary leakage vortex is seen as a large-scale region of positive signed vorticity on all slices. On slices forward of the blade trailing edge, the duct boundary layer is visible as a very thin sheet of negative signed vorticity at the domain's outer radial extent. Thus, the counter-rotating vorticity originates in the duct boundary layer in the reversed leakage flow. As the blade rotates (into the page), the adverse pressure gradient driving the leakage flow is removed. The duct boundary layer vorticity rolls up into a coherent vortex and migrates down from the duct wall farther behind the blade trailing edge. As the counter-rotating vorticity moves off the wall, it breaks up into smaller scale structures, which become intertwined with the small-scale positive signed vorticity of the separation sheet. The time taken for counter-rotating vortices to move downwards in the radial direction and for separation sheet vortex structures to traverse over top of the leakage vortex results in the small-scale interactions of corotating and counter-rotating vortices occurring between 20 % and 40 % of the chord length aft of the blade trailing edge. At the farthest slice aft of the blade trailing edge, most of the strong corotating vorticity has merged into the primary leakage vortex core. The vortex merger process observed in the present LES closely resembles that of the axial waterjet pump studied by Wu *et al.* (2011*a,b*, 2012). The breakup of negative signed azimuthal vorticity into smaller scales as a result of its interaction with the positive signed azimuthal vorticity of the separation sheet also mirrors the conclusions of Ortega *et al.* (2003).

The interactions of vortex structures are quantified using the decomposition of the vorticity transport equation in stretching, tilting and diffusion terms of Zhang *et al.* (1999). The vortex stretching term is $\boldsymbol{\omega} \cdot \boldsymbol{S} \cdot \hat{\boldsymbol{e}}_{\omega}$ where $\boldsymbol{\omega}$ is the vorticity vector, $\boldsymbol{S}$ is the strain rate tensor and $\hat{\boldsymbol{e}}_{\omega}$ is the unit vector aligned with the local axis of vorticity. Positive values indicate vorticity undergoing axial extension, while negative values are indicative of vortex compression. Vortex stretching is plotted in figure 14(*b*). Large positive stretching magnitudes are seen throughout the blade boundary layer and separation sheet forward of the trailing edge ($R\theta/c \leqslant 0$), as is intuitively expected given the large velocity gradients in that region. Immediately aft of the blade trailing edge ($R\theta/c = 0.11$), the thin region of
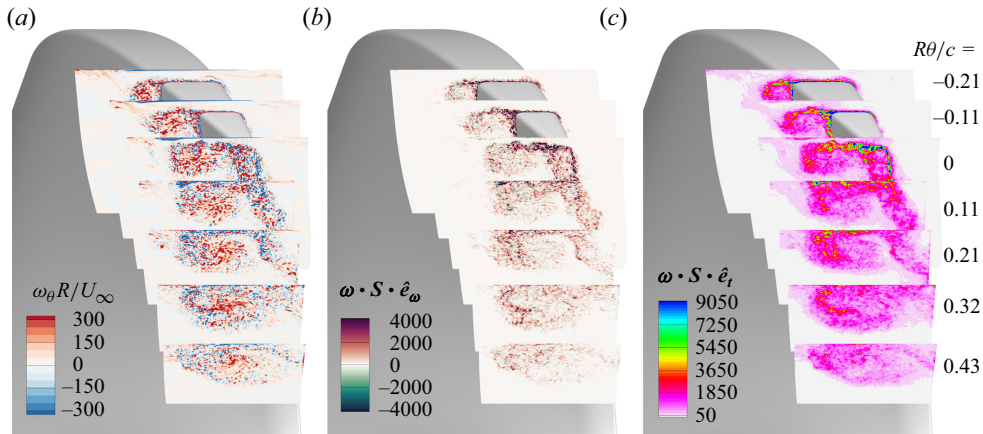
Figure 14. Instantaneous flow field on $x-r$ slices at $R\theta/c = -0.21, -0.11, 0.00, 0.11, 0.21, 0.32$ and 0.43. Colour contours are (*a*) azimuthal vorticity component $\omega_\theta R/U_\infty$, (*b*) vortex stretching and (*c*) vortex tilting.

sustained high stretching of the separation sheet scatters into smaller scale regions. At the second slice aft the trailing edge ($R\theta/c = 0.21$), the highest vortex stretching occurs near the duct wall in the region coinciding with the separation sheet vortex structures traversing over the primary leakage vortex and meeting the counter-rotating vorticity of the leakage flow duct boundary layer. Farther aft at $R\theta/c = 0.32$, where negative-signed vorticity from the leakage boundary layer has migrated off the duct wall, strong vortex stretching is seen again at the upstream periphery of the primary leakage vortex. This strongest vortex stretching far behind the blade occurs in an area nearer to the persistent low pressure of the primary vortex core than the strong stretching observed farther forward in the separation sheet. This observation highlights that extreme low-pressure events leading to cavitation inception are a multiscale phenomenon driven by both highly local stretching between corotating and counter-rotating small-scale vortices and the more persistent low-pressure regions driven by rotational flow at larger scales.

To the authors' knowledge, this is the first time that the cavitation inception mechanisms hypothesised by Chesnakas & Jessup (2003) have been evaluated quantitatively in the literature. More specifically, the present results find support for their hypothesis in the following ways: (i) strong vortex stretching persists far downstream ($R\theta/c > 0.30$) to where inception was observed; (ii) strongest stretching driving inception occurs at small length scales. In addition, the present results extend the previous hypotheses of ducted propulsor cavitation by highlighting that the leakage flow duct boundary layer rollup is an important source of secondary vorticity, while Chesnakas & Jessup (2003) highlights the role of trailing edge vortex shedding.

Figure 14(*c*) shows the vortex tilting term $\boldsymbol{\omega} \cdot \boldsymbol{S} \cdot \hat{\boldsymbol{e}}_t$. The vortex tilting is highest in the separation sheet aft the primary leakage vortex separation point, providing quantitative evidence to support the qualitative claims about blade tip vorticity realignment made in the discussion of figure 13. Unlike the stretching term, the vortex tilting term does not recover similar magnitudes to the separation sheet in the vortex interactions that occur farther behind the blade trailing edge.

The overall picture of vortex interactions in the wake of a ducted propulsor suggested by LES consists of corotating and counter-rotating small-scale vortices from the leakage flow, separation sheet, trailing edge wake and induced upstream vortex. A schematic illustration of the significant vortex flow structures suggested by the current LES is presented in figure 15(*a*). The blade is viewed from above the tip looking down at the trailing edge
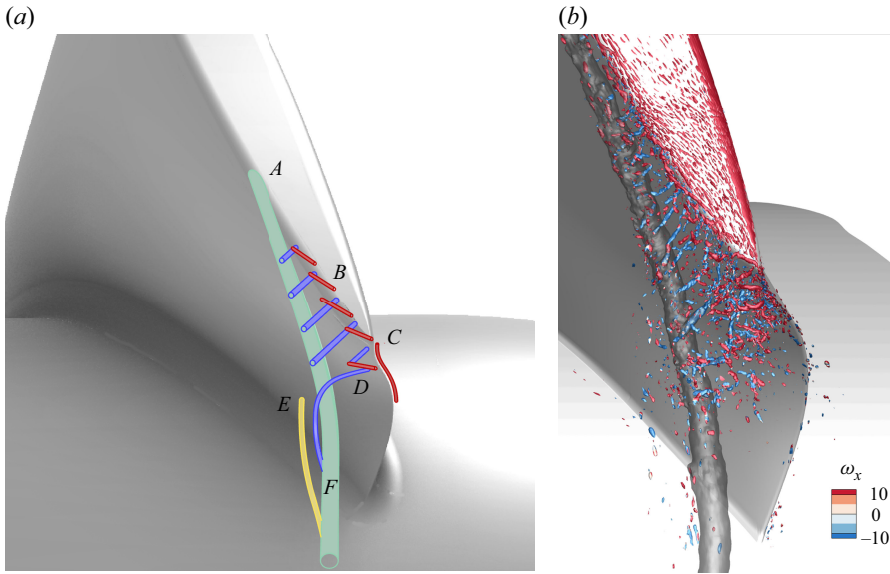
Figure 15. (*a*) Schematic of significant vortex structures in the ducted propeller flow near peak efficiency. Green represents the primary leakage vortex; red represents vortices perpendicular to the leakage flow originating in the blade boundary layer; blue represents the leakage-flow aligned vortices of the separation sheet; yellow is the induced counter-rotating vortex. (*b*) Isosurfaces of instantaneous $QR^2/U_\infty^2 = 170000$ from the LES Grid 2 solution coloured by the axial vorticity. An isosurface of $C_p = -4.7$ is also shown to denote the primary leakage vortex core.

such that the blade rotates upwards in the plane of the page. The primary leakage vortex is illustrated in green and detaches from the blade upstream from the trailing edge (*A*). Aft of the primary leakage vortex separation, additional vorticity of the blade tip boundary layer is shed and forms a separation sheet (*B*). The separation sheet is composed of vortices both perpendicular to the leakage flow (red) and parallel to the leakage flow (blue). At the trailing edge, additional vorticity is shed from the blade pressure side boundary layer (*C*). After the blade passes, the vortex structures of the separation sheet and boundary layer move above the primary leakage vortex (*D*). The rollup of the leakage flow duct boundary layer induces a counter-rotating vortex parallel to the primary vortex and upstream in the axial direction, which is shown in yellow (*E*). Far behind the blade trailing edge, vortex structures from the separation sheet and duct boundary layer rollup break up into smaller scales before eventually merging with the primary leakage vortex at the upstream periphery (*F*). Figure 15(*b*) repeats figure 13(*c*), but showing the Grid 2 solution rather than Grid 3. The coarser grid solution is presented here to remove the chaotic smaller scale turbulent structures for clarity. The same viewing angle as the schematic illustration in figure 15(*a*) is used in figure 15(*b*). The separation sheet vortex structures both aligned and perpendicular are clearly visible. The complex trailing edge wake shows vortical structures of opposing signs intertwined.

This section has provided a more detailed picture of the instantaneous tip vortex flow field than that provided by Chesnakas & Jessup (2003) and Oweis *et al.* (2006*a*). A large-scale coherent vortex emanating from the blade trailing edge is not seen in the instantaneous LES pressure field or Q-criterion. Rather, instantaneous vortex structures aligned with the tip leakage flow were observed throughout the separation sheet connecting the separated primary leakage vortex core to the blade tip boundary layer. These leakage flow-aligned structures are observed both forward and aft of the blade trailing edge and
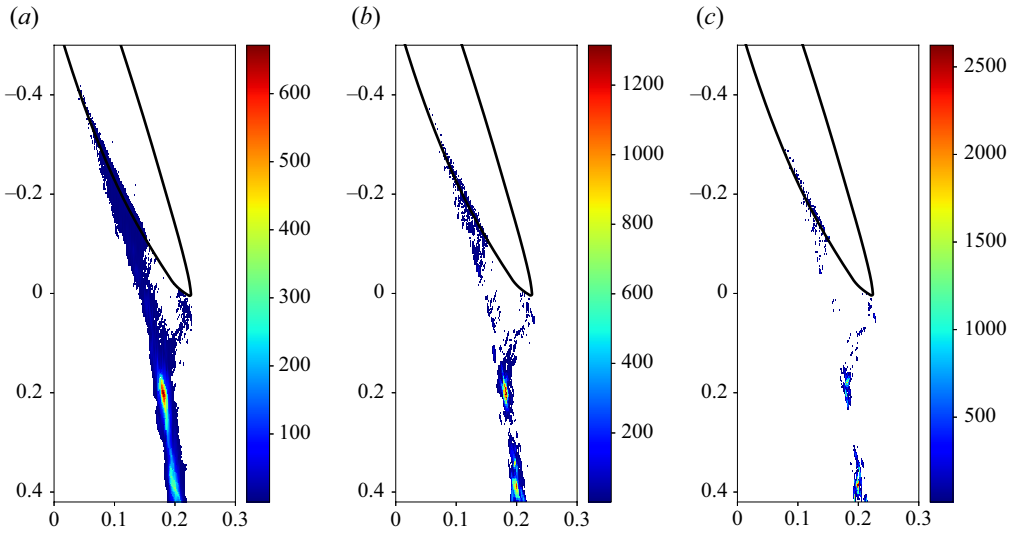
Figure 16. The joint PDF of low-pressure events in $x - \theta$ space for the LES solution on Grid 3 for (a) $C_p < -6.2$, (b) $C_p < -7.2$ and (c) $C_p < -7.8$. The blade outline is shown as a solid black line.

are found to correlate with side lobes of low-pressure wrapping around the primary vortex core. This suggests that the trailing edge vortex discussed by Chesnakas & Jessup (2003) and Oweis *et al.* (2006*a*) is not generated by the blade trailing edge itself but within the separation sheet. Despite offering a somewhat different description of the relevant mechanisms driving the flow, the current LES results find agreement with the experimental observation that secondary vortex structures near the blade trailing edge were likely to cavitate during the merger process with the primary vortex, as evidenced by the statistics of low-pressure events, that are presented in § 3.4.

3.4. *Low-pressure event statistics*

To estimate the probable location of cavitation inception, locations of extreme low-pressure events are collected for Grid 3 over 3.5 propeller revolutions. Low-pressure events are defined as any simulation control volume with an instantaneous C_p less than some threshold value and is sampled every 40 simulation time steps to ensure events are statistically independent in time. The joint probability density function (PDF) in $x - \theta$ space is shown in figure 16 for various threshold values: (figure 16*a*) $C_p < -6.2$, (figure 16*b*) $C_p < -7.2$ and (figure 16*c*) $C_p < -7.8$. The joint PDF is defined discretely by binning low-pressure events into discrete regions of $x - \theta$ space and dividing the number of samples in each bin by the total number of samples and the bin area. The normalisation of the PDF is completed separately for each threshold value of C_p. Lower pressure events are increasingly rare and, as a result, show less smooth distributions in the joint PDF for a given simulation sampling time interval. The event rates for the present results are N_{events}/blade-revolution = (figure 16*a*) 1.2×10^6, (figure 16*b*) 4.4×10^4 and (figure 16*c*) 5.4×10^3. The joint PDF of $C_p < -6.2$ in figure 16(*a*) shows a clear bimodal distribution, with low-pressure events more likely to occur in the trailing edge wake crossover region at $R\theta/c = 0.2$ and farther downstream at $R\theta/c = 0.4$ where high vortex stretching events were observed in figure 14(*b*). Low-pressure events are also seen to occur in the leakage vortex core and separation sheet structures forward of the blade trailing edge but at a much lower frequency than the vortex interaction regions in the blade wake.
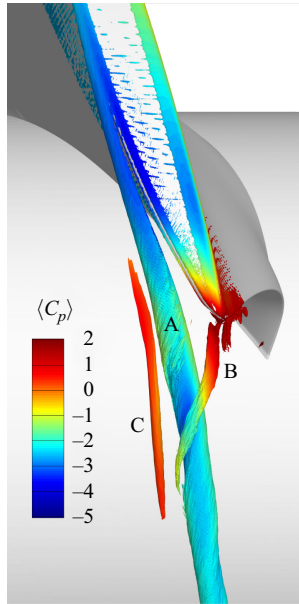
Figure 17. Isosurface of mean Q-criterion coloured by mean pressure coefficient. Only the tip region $r/R > 0.85$ is shown for clarity.

Furthermore, as the pressure threshold is decreased in figures 16(*b*) and 16(*c*) the probability density decays more significantly in the leakage vortex forward of the trailing edge than in the peak regions aft the blade trailing edge at $R\theta/c = 0.2$ and 0.4. This follows the experimental observations of Chesnakas & Jessup (2003) who observed cavitation inception at 50 % chord length aft, then, as the tunnel pressure was decreased, observed cavitation in secondary vortex structures closer to the trailing edge before the primary leakage vortex core cavitates as seen in figure 4(*a*). Joint PDFs for all three C_p thresholds do indicate the presence of such low-pressure trailing edge vortices, but at a much lower frequency than in the downstream regions.

As discussed in reference to figure 13, the trailing edge wake is composed of highly unsteady small-scale vortical structures of differing signs of rotation. The statistics of extreme low-pressure events suggest that these small-scale vortical structures may intermittently align such that a low-pressure region does occurs in the trailing edge wake. However, the trailing edge low-pressure region is not a persistent feature that can be visualised in the pressure field at any given time instant, such as that shown in figure 12.

3.5. *Mean flow field*

This section examines the time-averaged flow field of the LES results on the finest discretisation (Grid 3) to provide a more in-depth explanation of the formation of instantaneous flow structures observed in the previous section. The average flow in inertial coordinates is computed in the frame of reference of the blade.

The time-averaged vortex structures are examined in figure 17 with isosurface of mean $QR^2/U_\infty^2 = 35$. The time-averaged flow reveals a coherent vortex emanating from the blade trailing edge (*B*) in addition to the primary leakage vortex (*A*), as observed by Chesnakas & Jessup (2003) and Oweis *et al.* (2006*a*). Unlike the instantaneous flow, no vortex structures are observed in the separation sheet between the primary leakage vortex detachment and the blade trailing edge. The trailing edge vortex remains at a

pressure higher than ambient (p_∞) until it crosses over top of the primary leakage vortex. The interaction between primary and trailing edge vortices in the crossover region is also associated with a reduction in the leakage vortex mean core pressure. The induced upstream counter-rotating vortex (C) is visible as a region of red to the left of the primary leakage vortex. Unlike what was seen instantaneously in figure 14(*a*), the time-averaged induced upstream vortex diffuses before it migrates towards the primary leakage vortex upper periphery. The Q-criterion also identifies the attached boundary layer on the blade tip as a result of streamlines following the surface curvature.

Figure 18 shows slices of the mean flow field oriented parallel to the $x-r$ plane at the blade trailing edge and separated by $\Delta(R\theta/c) \approx 0.07$. Figure 18(*a*) colours the slices by the azimuthal component of vorticity. The primary vortex core is visible as a region of strong positive azimuthal vorticity which originates near the midchord at the blade suction side tip. The primary vortex core is seen to separate aft of the midchord but upstream of the trailing edge and is offset in the axial direction. The separation sheet connecting the separated primary leakage vortex core is visible as another region of strong positive azimuthal vorticity. Aft of the trailing edge, the separation sheet rolls up into a second coherent vortex corotating with the primary leakage vortex. The pressure side blade wake is visible as a sheet of strong counter-rotating vorticity. The upstream-induced vortex is also visible as a region of strong counter-rotating vorticity located above the primary vortex core in the radial direction. The induced vortex originates from the rollup of the tip leakage flow duct boundary layer after the blade passes by, as discussed in § 3.3. The rollup can be explained by the removal of the strong adverse pressure gradient created by the blade's passage which generates the reversed leakage flow in the tip gap. To more clearly delineate the boundaries of each vortex structure, isolines of the mean Q-criterion $=20$ and 220 are also shown as black lines on each slice.

Comparison of figures 17 and 18(*a*) with figures 13 and 14(*a*) suggests the following differences between the instantaneous and time-averaged flow: (i) in the time average flow, the upstream induced counter-rotating vortex diffuses before migrating away from the duct wall to the primary leakage vortex periphery, and (ii) the coherent corotating trailing edge vortex in the time-average flow is instantaneously a mixture of corotating and counter-rotating small-scale rotation. The strongest mean vortices are both corotating while the instantaneous flow has both corotating and counter-rotating vortices, whose interaction (mutual stretching) is stronger than corotating vortex merger. The importance of these vortex dynamics to the cavitation inception behaviour is revealed by the analysis of the vortex stretching term in discussion of figure 14(*b*).

Figure 18(*b*) shows slices coloured by the mean pressure coefficient. A strong pressure gradient across the tip gap can be seen, which is driving the leakage flow. The location of the primary leakage vortex core seen in figure 18(*a*) coincides with a strong low pressure, as expected. Outside the vortex core, the suction side region of the blade is below p_∞ forward of the trailing edge ($s < 0$) but above p_∞ aft of the trailing edge ($s > 0$). This is relevant for cavitation prediction in the sense that an idealised vortex model (such as that employed by Chesnakas & Jessup (2003) and Oweis *et al.* (2006*a*)) links vortex circulation to the pressure differential between the core and local ambient pressure. For the core to be at vapour pressure, the circulation of an idealised vortex would need to be larger aft of the trailing edge than it would forward nearer to the blade suction peak. The LES results show that vorticity is constantly being fed into the primary leakage vortex from the blade tip boundary layer and separation sheet, which causes the primary vortex to strengthen in circulation as s increases. This tradeoff between the increasing ambient pressure and increasing circulation with increasing s could potentially explain the lower event rates in the primary leakage vortex core near the trailing edge seen in figure 16.
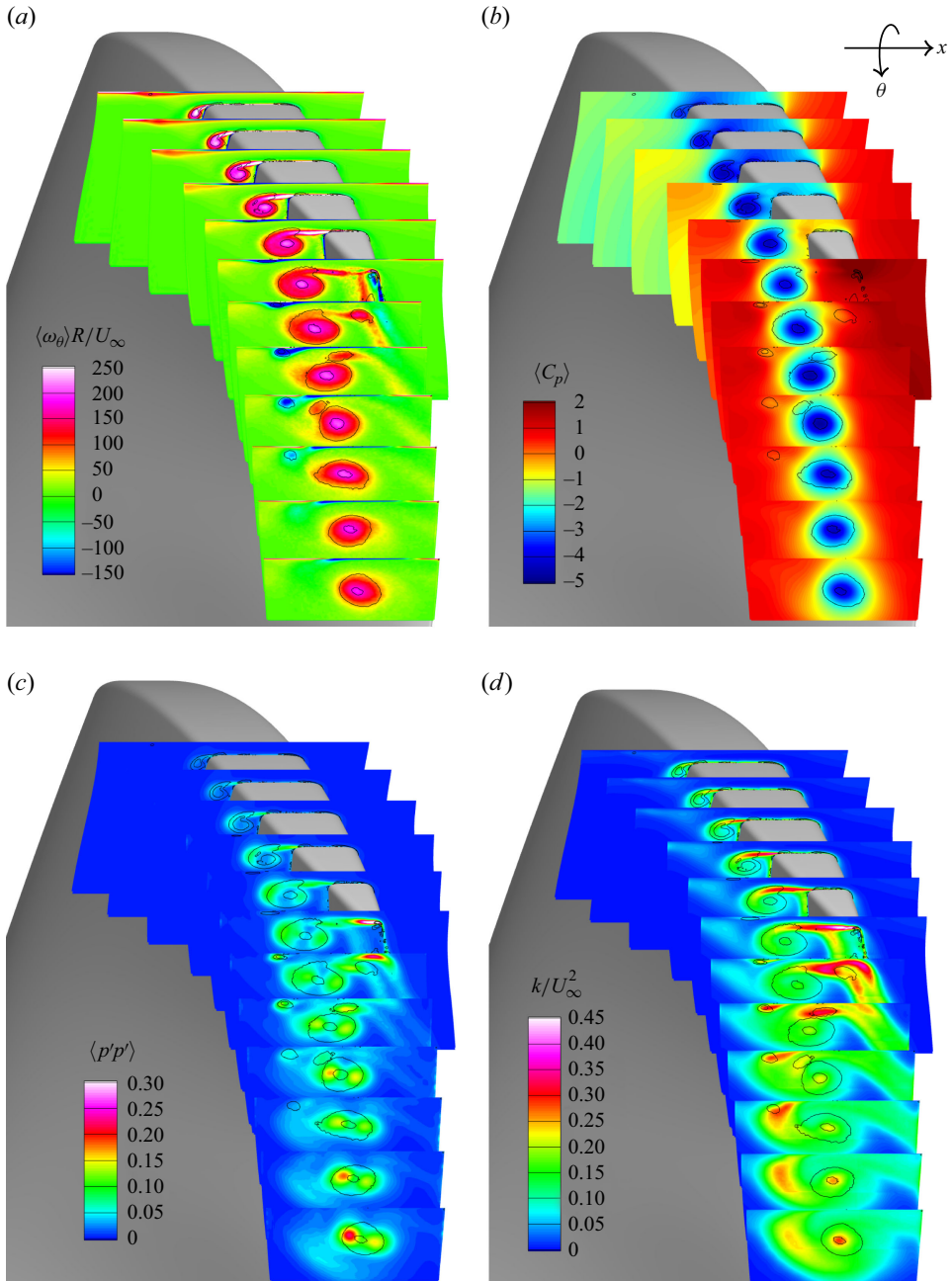
Figure 18. Slices through the time-averaged LES flow field computed on Grid 3 at $J = 0.98$ coloured by (*a*) azimuthal vorticity $\langle \omega_\theta \rangle$, (*b*) pressure coefficient $\langle C_P \rangle$, (*c*) mean-square pressure fluctuation $\langle p'p' \rangle$, (*d*) turbulent kinetic energy k.

Figure 18(*c*) displays the mean-square pressure fluctuation, which is a measurement of the unsteadiness of the vortex structures seen in the mean flow field in figure 18(*a*). Regions of high $\langle p'p' \rangle$ are visible in the primary separation sheet, the blade tip trailing edge region and on either side in the axial direction of the primary leakage vortex core moving aft. This is indicative of instantaneous vortices orbiting around the primary
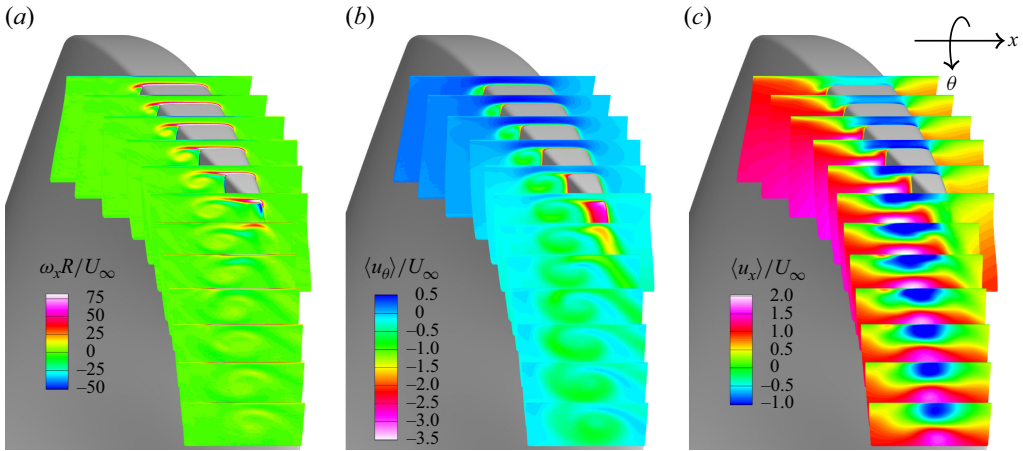
1010 A51-24

Figure 19. Slices through the time-averaged LES flow field computed on Grid 3 at $J = 0.98$ coloured by (a) azimuthal vorticity $\langle \omega_\theta \rangle$, (b) azimuthal velocity $\langle u_\theta \rangle$ and (c) axial velocity $\langle u_x \rangle$.

leakage vortex core, which is consistent with the interactions of small-scale vortex structures discussed earlier. More specifically, the observation of high mean-square pressure in the blade tip trailing edge provides evidence that the observed coherent trailing edge vortex observed in the experiments of Chesnakas & Jessup (2003) and Oweis *et al.* (2006*a*) is specifically a mean-flow phenomenon and that secondary vortices observed to cavitate during interaction with the primary leakage vortex may originate anywhere in the separation sheet connecting the blade tip boundary layer to the primary core. The large increase of $\langle p'p' \rangle$ on the upstream periphery of the vortex far aft of the blade trailing edge suggests that vortex core pressure minimum wanders in the axial direction. The regions of high $\langle p'p' \rangle$ correspond closely with the largest local $\partial \langle P \rangle / \partial x$ at $R\theta/c > 0.3$.

Figure 18(*d*) shows the turbulent kinetic energy field. Forward of the blade trailing edge, k is seen to peak in the upper periphery of the primary leakage vortex. As the primary leakage vortex moves away from the suction side blade tip, k remains high throughout the separation sheet. Immediately behind the blade trailing edge, high turbulence levels are seen in the suction side blade wake and the primary leakage vortex outer periphery. Turbulence associated with the counter-rotating duct boundary layer rollup begins at the blade trailing edge and increases with additional distance aft the trailing edge. At the last slice, turbulence levels at the vortex periphery begin to dissipate and k becomes highly concentrated in the primary leakage vortex core. High turbulence levels in the mean vortex core were also reported by Wu *et al.* (2012) in the axial waterjet experiment.

3.5.1. *Separation sheet skew*

The mean flow also provides insight into the production of vortices aligned with the leakage flow, which were observed to wrap helically around the primary vortex in the preceding § 3.3. Figure 19(*a*) reveals that the entire separation sheet is a location of high axial vorticity which is not present in other regions of the flow. Figure 19 also shows the contours of the mean azimuthal velocity (figure 19*b*) and axial velocity (figure 19*c*) in the inertial frame. In addition to the primary shear in the axial flow (dU_x/dr), there is also a secondary shear in the azimuthal flow (dU_θ/dr), representing a skewed shear layer. Skewed shear layers are a well-studied phenomenon and are known to produce vorticity aligned with the local flow (Lu & Lele 1993; Fiedler *et al.* 1998; Saric *et al.* 2003; Wernz *et al.* 2006; Meldi *et al.* 2020). Additionally, skewed shear layers have
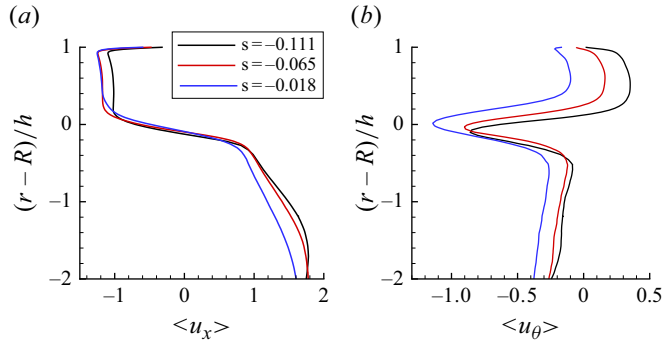
Figure 20. Mean velocity profiles across the separation sheet connecting the primary vortex core to blade tip boundary layer (*a*) axial velocity $\langle u_x \rangle / U_\infty$ and (*b*) azimuthal velocity $\langle u_\theta \rangle / U_\infty$.

an instability associated with the inflection point of the velocity profile. Profiles of mean flow components across the separation sheet are shown in figure 20. Profiles are extracted in the radial direction at three locations upstream from the trailing edge $R\theta/c = -0.018, -0.065, -0.111$ and located halfway between the blade suction side and the primary leakage vortex core in the x-direction. The vertical axis shows the radial coordinate normalised by the tip gap size h and centred on the blade tip at $r = R$. Above the separation sheet in the tip leakage flow, the axial velocity is strongly negative and the azimuthal velocity is moderately positive (moving opposite to the blade). The azimuthal velocity is moving with the blade just at the blade tip $r/R = 1$ because fluid at this location originates in the blade boundary layer before separating off the suction side blade tip. Below the separation sheet, the azimuthal velocity is moderately negative (moving with the blade) while the axial velocity is strongly positive due to the radial circulation (or lift) produced by the blade passage. The relative strength of the flow components changes significantly with s in the tip leakage flow, with profiles closer to the trailing edge having weaker azimuthal velocity and stronger axial velocity. Below the separation sheet, the dependence on s is weaker. The axial velocity profile has a single inflection point at $r/R = 0.998$ while the azimuthal velocity profile has two inflection points at $r/R = 1.002$ and 0.995, respectively.

The impact of the skew of the shear layer on turbulent structures is clearly visible in the Reynolds stress tensor components displayed in figure 21. Figure 21(*a*) displays slices of $\langle u'_x u'_r \rangle$ which demonstrates that in the separation sheet, the axial and radial velocity fluctuations are positively correlated. Meanwhile, figure 21(*b*) shows that the radial and azimuthal velocity fluctuations $\langle u'_r u'_\theta \rangle$ are also positively correlated. Together, this provides evidence of instantaneous vortices that are corotating with the primary vortex but with a vortex core somewhat aligned with the axial direction, confirming the observations made in figure 13(*b*). Figure 21(*c*) shows that correlation of $\langle u'_x u'_\theta \rangle$ flips sign on either side of the separation sheet. Above the separation sheet in the radial direction, fluctuations are positively correlated, while below the separation sheet, they are negatively correlated. However, correlations of $\langle u'_x u'_\theta \rangle$ are approximately two times smaller than correlations of either $\langle u'_x u'_r \rangle$ or $\langle u'_r u'_\theta \rangle$ in the separation sheet, indicating that instantaneous vortices in this region are unlikely to have a core aligned with the radial direction. This is the expected result given that the mean shear of the separation sheet is much larger in the radial direction. The regions of largest $\langle u'_x u'_\theta \rangle$ are instead found in the blade suction side boundary layer and wake where the dominant shear is in the axial direction.
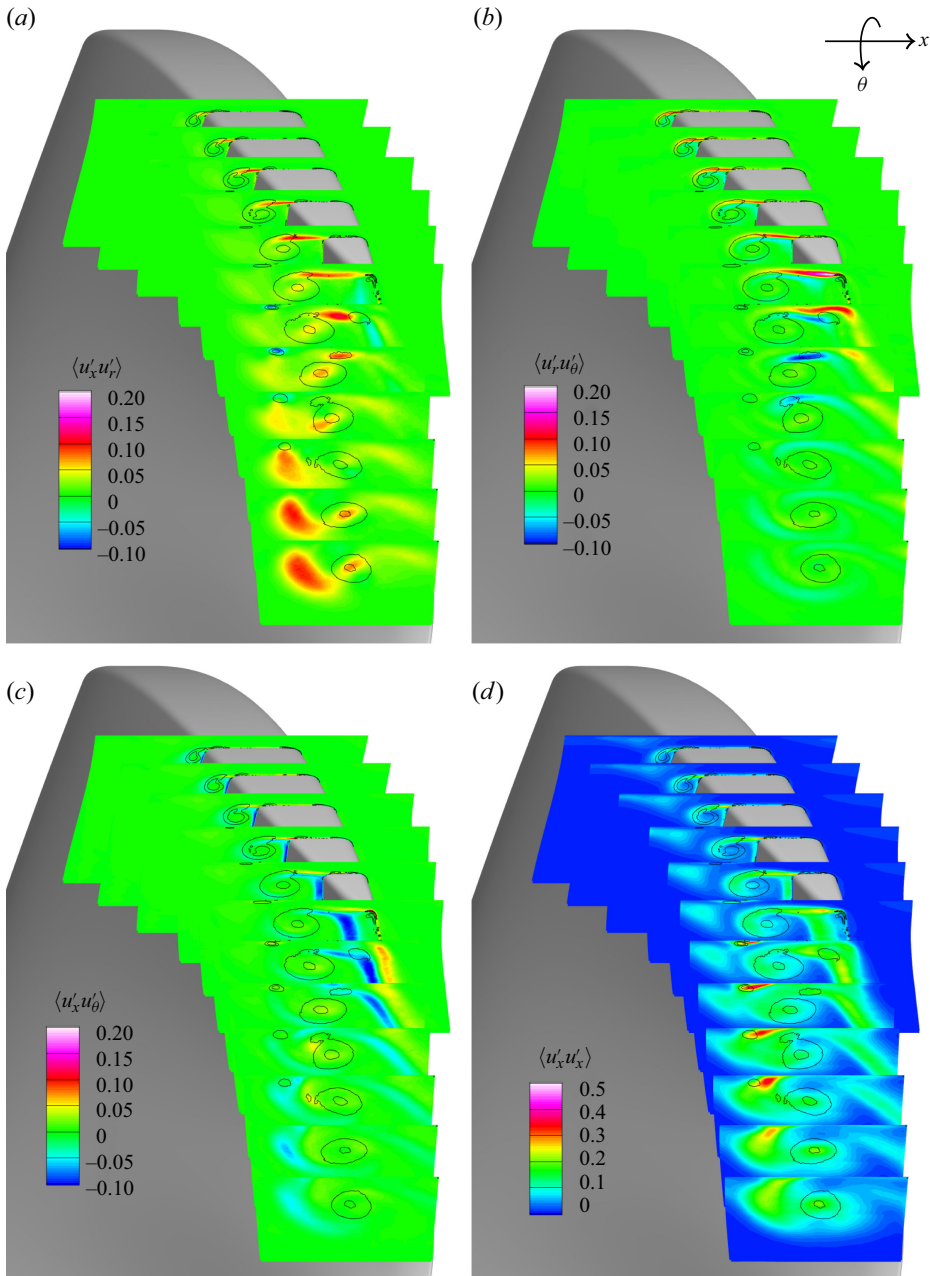
Figure 21. Reynolds stress tensor components from the LES Grid 3 solution at $J = 0.98$. Slices are parallel to the $x-r$ plane at the blade trailing edge and coloured by (*a*) $\langle u'_x u'_r \rangle$, (*b*) $\langle u'_r u'_\theta \rangle$, (*c*) $\langle u'_x u'_\theta \rangle$ and (*d*) $\langle u'_x u'_x \rangle$. The flow field quantities are normalised appropriately using ρ, U_∞ and R.

Finally, figure 21(*d*) shows that the area between the induced upstream vortex and the edge of the primary leakage vortex is associated with a region of high turbulent fluctuation in the axial flow, $\langle u'_x u'_x \rangle$. This indicates that this vortex is closely associated with the interaction of the tip leakage flow in the negative x-direction and the incoming turbulent duct boundary layer in the positive x-direction. A similar observation was made in the

1010 A51-27

axial waterjet experiments of Wu *et al.* (2012). This conclusion suggests that simulations performed with a steady or laminar inflow to the propulsor could predict a different vortex structure in the blade wake. Additionally, this suggests that the thickness of the duct boundary layer relative to the tip gap spacing could be an important scaling parameter that is non-trivial to achieve when comparing across experimental facilities.

In this section, mean flow features driving tip vortex structures for a ducted rotor at $J = 0.98$ have been examined. The coherent trailing edge vortex described by Chesnakas & Jessup (2003) was revealed in the LES results to be a feature of large-time averages of the small-scale vortices in the region. Meanwhile, instability mechanisms not previously identified in the ducted propulsor flow were observed in the separation sheet connecting the blade tip boundary layer to the separated primary leakage vortex core. The importance of these instability mechanisms to the vortex structures of the separation sheet discussed in § 3.3 was shown in the off-diagonal terms of the Reynolds shear stress.

4. Conclusion

Unstructured overset LES is used to study the tip leakage flow and vortex structures of the ducted propeller P5407. The overset method enables the creation of fully hexahedral and high-resolution grids that represent and capture the complex geometries of the rotor blades and duct locally. The sensitivity of the propeller thrust K_T to the inflow was observed and quantified near $J = 1.11$. At design advance ratio $J = 0.98$, LES predicts the propeller loads within the experimental scatter when matching the incoming mass flow rate. The time-averaged flow field is compared with experimental LDV, showing agreement in the mean tip vortex strength and position.

Assessing the pressure field reveals a strong leakage vortex that separates forward of the trailing edge, as observed in the experiments. On the other hand, no persistent vortex is found to emanate from the trailing edge. Rather, the trailing edge flow is found to instantaneously be composed of a complex mixture of small-scale vortices of differing sign of rotation. The leakage flow generates rolling vortices in the blade boundary layer oriented perpendicular to the leakage flow. The leakage flow then separates off the suction side blade tip resulting in the rollup of the primary leakage vortex. Aft of the primary leakage vortex separation point, a separation sheet connects the primary core to the blade tip boundary layer. The separation sheet is shown to resemble a skewed mixing layer with two inflection points in the velocity profiles representing a source of instability in the flow not previously identified in the literature. The separation sheet is seen to contain instantaneous vortices aligned with the leakage flow. Analysis of the vortex tilting term confirms that blade-tip boundary layer structures are reoriented in this region to align more with the axial direction. The orbit and merger of vortices from the separation sheet into the primary vortex core is seen to induce side-lobes of low-pressure wrapping helically around the primary vortex core both forward and aft of the trailing edge. These small-scale structures do not immediately merge with the primary vortex, but rather traverse over top of the leakage vortex before meeting the incoming bulk flow. Counter-rotating vorticity from the leakage flow duct boundary layer is also seen to rollup and interact with the separation sheet structures in the same region. The stretching induced by these vortex interactions is quantified and seen to increase as counter-rotating vortex structures migrate down from the duct wall. The relevance and statistical significance of these small-scale instantaneous vortex observations is quantified in terms of the off-diagonal Reynolds stresses and mean-square pressure fluctuations.

Statistics of the instantaneous extreme low-pressure events show the highest likelihoods of cavitation inception between $20\,\%$ and $40\,\%$ of the tip chord length aft of the

trailing edge. Secondary low-pressure structures closer to the trailing edge are also observed to reach extreme low pressures, but at a much lower frequency than regions farther behind the blade. The present results therefore find support for the inception mechanisms hypothesised by Chesnakas & Jessup (2003) in the following ways: (i) strong vortex stretching persists far downstream ($R\theta/c > 0.30$) to where inception was observed; (ii) strongest stretching driving inception occurs at small length scales. In addition, the present results extend the previous hypotheses of ducted propulsor cavitation by highlighting that the leakage flow duct boundary layer rollup is an important source of secondary vorticity.

Declaration of interests. The authors report no conflict of interest.

REFERENCES

BREWER, W.H. 2002 *On Simulating Tip-Leakage Vortex Flow to Study the Nature of Cavitation Inception*. Mississippi State University.

CHESNAKAS, C.J. & JESSUP, S.D. 2003 Tip-vortex induced cavitation on a ducted propulsor. In *Fluids Engineering Division Summer Meeting*, pp. 257–267. American Society for Mechanical Engineers.

DUBIEF, Y. & DELCAYRE, F. 2000 On coherent-vortex identification in turbulence. *J. Turbul.* **1**, N11.

FIEDLER, H.E., NAYERI, C., SPIEWEG, R. & PASCHEREIT, C.O. 1998 Three-dimensional mixing layers and their relatives. *Expl Therm. Fluid Sci.* **16** (1), 3–21.

GERMANO, M., PIOMELLI, U., MOIN, P. & CABOT, W.H. 1991 A dynamic subgrid–scale eddy viscosity model. *Phys. Fluids A* **3** (7), 1760.

HORNE, W.J. & MAHESH, K. 2019a A massively-parallel, unstructured overset method for mesh connectivity. *J. Comput. Phys.* **376**, 585–596.

HORNE, W.J. & MAHESH, K. 2019b A massively-parallel, unstructured overset method to simulate moving bodies in turbulent flows. *J. Comput. Phys.* **397**, 108–790.

HORNE, W.J. & MAHESH, K. 2021 A hardware accelerated unstructured overset method to simulate turbulent fluid flow. *J. Comput. Phys.* **444**, 110574.

HSIAO, C.T. & CHAHINE, G.L. 2006 Effect of unsteady turbulent fluctuations on vortex/vortex/nuclei interactions. In *26th Naval Hydrodynamics Symposium, Rome, Italy*. Office of Naval Research.

HSIAO, C.-T. & CHAHINE, G.L. 2008 Numerical study of cavitation inception due to vortex/vortex interaction in a ducted propulsor. *J. Ship Res.* **52** (02), 114–123.

HUNT, J.C.R., WRAY, A.A. & MOIN, P. 1988 *Eddies, Streams, and Convergence Zones in Turbulent Flows*. Center for Turbulence Research Report CTR-S88.

JUDGE, C.Q., OWEIS, G.F., CECCIO, S.L., JESSUP, S.D., CHESNAKAS, C.J. & FRY, D.J. 2001 Tip-leakage vortex inception on a ducted rotor. In *CAV 2001: Fourth International Symposium on Cavitation*. University of Michigan.

KIM, J., PATERSON, E.G. & STERN, F. 2006 Rans simulation of ducted marine propulsor flow including subvisual cavitation and acoustic modeling. *J. Fluids Engng* **128** (4), 799–810.

KROLL, T., MORSE, N., HORNE, W. & MAHESH, K. 2020 Large eddy simulation of marine flows over complex geometries using a massively parallel unstructured overset method. In *Proceedings of the 33rd Symposium on Naval Hydrodynamics, Osaka, Japan*. Office of Naval Research.

KROLL, T.B. & MAHESH, K. 2022 Large-eddy simulation of a ducted propeller in crashback. *Flow* **2**, E–4.

KUMAR, P. & MAHESH, K. 2017 Large eddy simulation of propeller wake instabilities. *J. Fluid Mech.* **814**, 361–396.

LILLY, D.K. 1992 A proposed modification of the Germano subgrid-scale closure method. *Phys. Fluids A* **4** (3), 633–635.

LU, G. & LELE, S.K. 1993 Inviscid instability of a skewed compressible mixing layer. *J. Fluid Mech.* **249**, 441–463.

MAHESH, K., CONSTANTINESCU, G. & MOIN, P. 2004 A numerical method for large–eddy simulation in complex geometries. *J. Comput. Phys.* **197** (1), 215–240.

MELDI, M., MARIOTTI, A., SALVETTI, M.V. & SAGAUT, P. 2020 Numerical investigation of skewed spatially evolving mixing layers. *J. Fluid Mech.* **897**, A35.

MIORINI, R.L., WU, H. & KATZ, J. 2012 The internal structure of the tip leakage vortex within the rotor of an axial waterjet pump. *J. Turbomach.* **50** (11), 2574–2587.

MORSE, N. & MAHESH, K. 2021 Large-eddy simulation and streamline coordinate analysis of flow over an axisymmetric hull. *J. Fluid Mech.* **926**, A18.

MORSE, N. & MAHESH, K. 2023*a* Effect of tabs on the shear layer dynamics of a jet in cross-flow. *J. Fluid Mech.* **958**, A6.

MORSE, N. & MAHESH, K. 2023*b* Tripping effects on model-scale studies of flow over the DARPA SUBOFF. *J. Fluid Mech.* **975**, A3.

ORTEGA, J.M., BRISTOL, R.L. & SAVAŞ, Ö. 2003 Experimental study of the instability of unequal-strength counter-rotating vortex pairs. *J. Fluid Mech.* **474**, 35–84.

OWEIS, G.F. 2003 An experimental investigation into the dynamics of propeller tip vortices and the associated cavitation noise. *PhD thesis*, University of Michigan, USA.

OWEIS, G.F., FRY, D., CHESNAKAS, C., JESSUP, S. & CECCIO, S.L. 2006*a* Development of a tip-leakage flow—part 1: the flow over a range of reynolds numbers. *J. Fluids Engng* **128** (4), 751–764.

OWEIS, G.F., FRY, D., CHESNAKAS, C., JESSUP, S. & CECCIO, S.L. 2006*b* Development of a tip-leakage flow. Part 2: comparison between the ducted and un-ducted rotor. *J. Fluids Engng* **128** (4), 765–773.

PARK, N. & MAHESH, K. 2009 Reduction of the Germano-identity error in the dynamic Smagorinsky model. *Phys. Fluids* **21** (6), 065106.

SARASWAT, A., PANIGRAHI, C. & KATZ, J. 2024 Experimental characterization of the evolution of flow and turbulence in the tip region of a ducted marine propeller. In *Proceedings of the 35th Symposium on Naval Hydrodynamics, Nantes, France*. Office of Naval Research.

SARIC, W.S., REED, H.L. & WHITE, E.B. 2003 Stability and transition of three-dimensional boundary layers. *Annu. Rev. Fluid Mech.* **35** (1), 413–440.

VERMA, A. & MAHESH, K. 2012 A Lagrangian subgrid-scale model with dynamic estimation of Lgrangian time scale for large eddy simulation of complex flows. *Phys. Fluids* **24** (8), 085101.

WERNZ, S., RINGWALD, H. & FASEL, H. 2006 Numerical investigation of instabilities in three-dimensional skewed shear layers. In *3rd AIAA Flow Control Conference*. American Institute of Aeronautics and Astronautics.

WU, H., MIORINI, R.L. & KATZ, J. 2011*a* Measurements of the tip leakage vortex structures and turbulence in the meridional plane of an axial water-jet pump. *Exp. Fluids* **50** (4), 989–1003.

WU, H., MIORINI, R.L., TAN, D. & KATZ, J. 2012 Turbulence within the tip-leakage vortex of an axial waterjet pump. *AIAA J.* **134** (11), 2574–2587.

WU, H., TAN, D., MIORINI, R.L. & KATZ, J. 2011 Three-dimensional flow structures and associated turbulence in the tip region of a waterjet pump rotor blade. *Exp. Fluids* **51** (6), 1721–1737.

ZHANG, C., SHEN, L. & YUE, D.K.P. 1999 The mechanism of vortex connection at a free surface. *J. Fluid Mech.* **384**, 207–241.